Ageing response and strengthening mechanisms in a new Al-Mn-Ni-Cu-Zr alloy designed for laser powder bed fusion

Maxence Buttard, Marti Lopez Freixes, Charles Josserond, Patricia Donnadieu, Béchir Chéhab, Jean-Jacques Blandin, Baptiste Gault, Frédéric de Geuser, Guilhem Martin

To cite this version:

Maxence Buttard, Marti Lopez Freixes, Charles Josserond, Patricia Donnadieu, Béchir Chéhab, et al.. Ageing response and strengthening mechanisms in a new Al-Mn-Ni-Cu-Zr alloy designed for laser powder bed fusion. Acta Materialia, 2023, 259, pp.119271. ⟨10.1016/j.actamat.2023.119271⟩. ⟨hal-04246654⟩

HAL Id: hal-04246654

https://hal.science/hal-04246654v1

Submitted on 17 Oct 2023

Ageing response and strengthening mechanisms in a new Al-Mn-Ni-Cu-Zr alloy designed for laser powder bed fusion

Maxence Buttard[1], Marti Lopez Freixes[2], Charles Josserond[1], Patricia Donnadieu[1], Béchir Chéhab[3], Jean-Jacques Blandin[1], Baptiste Gault[2,4], Frédéric De Geuser[1], Guilhem Martin[1]

1.Univ. Grenoble Alpes, CNRS, Grenoble INP, SIMAP, F-38000 Grenoble

2. Max-Planck-Institut für Eisenforschung, Max-Planck-Str. 1, 40237, Düsseldorf, Germany

3. Constellium Technology Center, Parc économique Centr'Alp, 725, rue Aristide-Bergès, CS 10027, 38341 Voreppe cedex, France

4. Department of Materials, Imperial College London, South Kensington, SW7 2AZ, UK

Abstract

Aluminum alloys designed for laser powder bed fusion (L-PBF) often show a bimodal grain structure and a strong out-of-equilibrium character with heterogeneities developing at scales ranging from the melt pool, i.e several hundred microns, down to sub-nanometer. When subjected to post-fabrication heat treatments, microstructural evolutions arise at all scales. Herein are established the relationships between microstructure and mechanical properties at room temperature of a novel Al-4Mn-3Ni-2Cu-1Zr alloy, designed for L-PBF and subjected to direct ageing. On the basis of a multiscale microstructural study using scanning-electron microscopy (SEM), automated orientation mapping in the transmission-electron microscope (TEM-ACOM), atom probe tomography (APT), and synchrotron small-angle X-ray scattering (SAXS), we discuss and weigh the role of multiple strengthening mechanisms to the high strength of the material. In the stress-relieved conditions (300°C/4h), the yield strength is about 320 MPa and solid solution strengthening accounts for nearly two third of the yield strength (~200 MPa) thanks to a very high content of Mn retained in solid solution (> 1.5 at.%) and, to a lesser extent, grain boundary strengthening. After ageing at 400°C/1h, the yield strength reaches 410 MPa. The additional contribution is brought by precipitation strengthening by $L1_2$-ordered Al_3Zr. The composite effect due to the large fraction of relatively fine (< 1 μm) intermetallic particles (~30%) is highlighted and cannot be neglected. This work provides guidelines to further optimize the mechanical properties and thermal stability of Al-alloys designed for L-PBF.

Keywords: Laser Powder Bed Fusion; Al alloys; Mechanical Properties; TEM; APT

1. Introduction

Aluminum alloys are good candidates for weight saving due to their high specific properties. Laser powder bed fusion (L-PBF) has emerged as a promising additive manufacturing method to produce sophisticated geometries and reach additional weight reduction for automobiles or aircraft [1,2]. However, traditional high-strength Al alloys from the 2XXX [3], 6XXX [4], or 7XXX series [5] suffer from severe hot cracking when processed by additive manufacturing. To overcome this issue, two solutions have been proven to be efficient so far. First, increasing the building plate temperature to 500°C [6] reduces the thermal stresses responsible for cracking, but this results in the loss of the desired out-of-equilibrium character of the resulting microstructure.

Second, grain refinement can alleviate hot cracking, since it helps to distribute thermal stresses over a larger number of interfaces. Several strategies have been proposed to promote the heterogeneous nucleation of Al grains at the melt-pool boundaries. The first strategy, inherited from casting, consists in the addition of extra particles such as TiB_2 [7] or CeB_6 [8] that act as direct nucleating agents. A second option involves the introduction of nanoparticles such as Zr-hydrides [5], [9], or Zr-oxides [10,11] which decompose during L-PBF processing thus adding Zr to the melt. Upon cooling, the $L1_2$-Al_3Zr phase precipitates in the liquid and promotes the nucleation of Al grains through a peritectic transformation. Another way to refine the grain size is to introduce directly to the nominal composition of the alloy elements known to form a primary $L1_2$-Al_3X phase, X = Zr [12–14], Sc, Ti [15,16], Ta [17], Nb [16,18,19]. This strategy is straightforward as the preliminary mixing stage is suppressed.

Beyond the mitigation of hot cracking, other criteria have been included when designing Al alloys for L-PBF, in particular, to leverage the out-of-equilibrium processing conditions. In this context, new Al alloys to be fabricated by L-PBF have been introduced, with reports of outstanding room temperature mechanical properties, see e.g. Scalmalloy [20], Al-Mn-Sc [21,22], Al-Mg-Si-Sc-Zr [23], Al-Zn-Mg-Cu-Sc-Zr [20]. Alloys with a superior strength - conductivity trade-off have also been designed [24,25].

Alloys with a high-volume fraction of intermetallic particles (>10%) or strengthened through high-temperature precipitation with thermally stable strengthening precipitates are often considered good candidates for high temperature applications (typically between 150 and 400°C). Additive manufacturing, and, in particular, L-PBF offers new opportunities to develop Al alloys for high-temperature applications. Indeed, the out-of-equilibrium processing conditions can be exploited to produce microstructures decorated with large fractions of fine intermetallic particles, or to achieve supersaturated solid solution of slow-diffusing solutes, such as Zr, known to form thermally stable precipitates upon ageing during a post-fabrication heat treatment. Those opportunities were recently emphasized by Michi et al. [26]. Alloys with substantial additions of Ce [27–32] and the Al-5Fe-6Cr also appear promising [33].

With the aim of designing an alloy that shows good mechanical properties with an enhanced thermal stability at room temperature (yield strength > 400 MPa) and that retains a relatively high strength (>250 MPa) at higher temperatures (150°C-300°C), the Al-Mn-Ni-Cu-Zr system was explored. These alloys can take advantage of thermally stable strengthening precipitates and also present a large fraction of relatively fine intermetallics. The rationale behind the selection of this system was introduced in Ref. [34] but is briefly recalled below. Alloying elements with high vapour pressure such as Mg or Zn, often used in traditional high-strength Al alloys, tend to increase process instabilities and a loss of such elements may ultimately lead to a reduced precipitation strengthening. These alloying elements were thus excluded. Using only alloying elements with low diffusivity in Al prevents precipitation during printing, which is done typically at 100-200°C.

Understanding the mechanical properties of Al alloys designed for L-PBF is a challenging task, especially as the inherited microstructures show a strong out-of-equilibrium character with heterogeneities developing across a wide range of scales. One can see a 3D arrangement of melt pools at the macroscale, with fine equiaxed grains at the melt boundaries and columnar growth at the center, see e.g. [13,20,23,24]. Variations in local solidification conditions also result in heterogeneities at the intragranular scale, with a distribution of intermetallic particles that may evolve in morphology, size or fraction across the melt pool [20]. Ultimately, changes in local solidification conditions may also result in heterogeneities at the atomic scale. Indeed, solute trapping becomes more significant at the upper part of the melt pool because of the increase in solid-liquid interface velocity [13,14]. Thus, local variations of the supersaturated solid solution cannot be excluded. When such complex microstructures are subjected to heat treatments, changes from the grain scale down to the atomic scale are expected [20,21]. Investigating the microstructure-property relationships in such materials thus requires the monitoring of microstructural changes from the macroscale down to the atomic scale to be able to weigh the multiple synergistic strengthening mechanisms [20,21,23,35].

The out-of-equilibrium processing conditions during L-PBF can be exploited to achieve supersaturated solid solutions, i.e beyond the solubility limits imposed by traditional processing routes, including a solution heat treatment. This idea questions the need for solutionizing and quenching prior to ageing. Here, two slow-diffusing solutes are included in the alloy composition, Mn and Zr. Mn is among the best solid solution strengtheners and shows some solubility in Al at the equilibrium (0.61 at.% in the binary system). The role of Zr is twofold, grain refinement via precipitation of the primary $L1_2$-Al_3Zr phase and strengthening by the precipitation of a dispersion of finer-scale Al_3Zr through post-fabrication ageing. Ni was also selected because of its low solubility in Al and its ability to form a variety of intermetallics, in particular with Cu, which was also added. High cooling rates during L-PBF are exploited to contribute to reinforcing the material by producing a network of fine (Ni, Cu)-rich intermetallics.

In this study, we focus on the evolution of the room-temperature mechanical properties of a new Al-4Mn-3Ni-2Cu-1Zr alloy designed for L-PBF and subjected to direct ageing at 400°C. The grain structure characterized using electron backscattered diffraction (EBSD) is not subjected to strong variations upon ageing at 400°C. Coarsening of intermetallic particles during ageing at 400°C is revealed using SEM imaging. The crystallography and chemistry of the various intermetallic compounds are investigated using X-ray diffraction (XRD) and electron dispersive spectroscopy (EDS) in the scanning and transmission electron microscope (SEM/TEM). The decomposition of the supersaturated solid solution inherited from L-PBF is monitored using automated orientation mapping in the TEM (TEM–ACOM), atom probe tomography (APT), and synchrotron small-angle X-ray scattering (SAXS). The mechanical properties measured after stress-relief heat treatment as well as after different ageing times at 400°C are discussed in light of the microstructural evolutions evidenced from the macroscale down to the atomic scale.

2. Experimental Procedures

2.1. Materials and L-PBF processing conditions

Table 1 gives the chemical composition of the as-received powder batch measured by inductively coupled plasma atomic emission spectroscopy (ICP-AES). Gas atomization was used to produce the pre-alloyed powder having a size distribution between 10 and 70 µm. A 400 W fiber laser with an 80 µm spot size was used in an EOS M290 L-PBF machine with high-purity argon (< 0.2% O_2) to fabricate cylindrical samples (11 mm in diameter and 60 mm in height). The samples were built using the following processing parameters: a power of 370 W, a scan speed of 1400 mm/s, a hatching distance of 110 µm, and a layer thickness of 60 µm. The scanning strategy uses 4 mm stripes in bi-directional scanning with a 67° rotation between each layer. Throughout the builds, the temperature of the building substrate was maintained at 100°C.

	Al	**Mn**	**Ni**	**Cu**	**Zr**
wt. %	Bal.	3.87	3.14	1.86	1.02
at.%	Bal.	2.01	1.53	0.84	0.32

Table 1 : Chemical composition of the pre-alloyed powder batch used in the present work given respectively in wt.% and at.%.

2.2. Heat treatments

Before removing samples from the building plate, a Stress Relief (SR) heat treatment was carried out under air at 300°C for 4h to release residual stresses arising from the L-PBF fabrication. Samples subjected to the SR heat treatment were then heat treated at 400°C to interrogate the ageing response of the investigated material. Different ageing times were investigated at 400°C, see **Table 2**. For the sake of clarity, the color code indicated in **Table 2** for the various heat treatments is used throughout the manuscript.

Heat Treatment	Temperature (°C)	Time (hours)
Stress Relief (SR) 🟢	300	4
SR+ 400°C/1h 🟡	400	1
SR + 400°C/4h 🟠	400	4
SR + 400°C/96h 🔴	400	96

Table 2 : Summary of the different heat treatments investigated.

2.3. Mechanical characterizations

The hardness was evaluated using a Tester FALCON 455 using a Vickers tip, a load of 30 kg, and a dwell time of 10 seconds. At least ten measurements have been conducted for each condition.

Tensile specimens were machined from L-PBF cylindrical specimens to prevent the possible detrimental impact of the initial roughness on the macroscopic tensile properties. The loading direction was aligned with the building direction. The tensile tests were performed on dog-bone cylindrical specimens with a gauge length of 24 mm and a diameter of 4 mm. The exact geometry is given in supplementary materials, see *Figure S 1*. Tensile tests were conducted at a constant strain rate $\dot{\varepsilon} = 10^{-4}$ s^{-1} on a MTS4M testing machine equipped with a 20kN cell force. Using two 6M-pixel cameras and the GOM software, the deformation was measured by digital image correlation. The conventional yield strength $\sigma_{y,0.2\%}$ was determined by measuring the true stress at 0.2% plastic strain

2.4. Microstructural characterizations

Samples for microstructural characterization were polished with SiC abrasive papers down to the P4000 grade, followed by a step using a 1 µm diamond suspension. A final vibratory polishing with a 0.03 µm colloidal silica solution was carried out using the Buehler VibroMet tool. The grain structure was examined after the different heat treatments using a Zeiss Gemini SEM 500 FEG equipped with an EBSD detector. To be statistically representative of the potential grain size evolution of the FCC-Al grains, large EBSD maps were collected in the samples subjected to the various heat treatments investigated in this work.

To investigate the microstructure at the micrometer scale, site-specific lift-outs using a focused ion beam (Zeiss NVision 40 Ga FIB-SEM) were performed to extract lamellae from regions of interest for TEM analysis. First, a 1 µm-thick lamella protected by carbon and platinum (total thickness 1 µm) was extracted from the bulk. Successive Ga milling was used to reduce the thickness of the lamella to less than 100 nm. The final thinning steps were carried out on both sides of the lamella at an accelerating voltage of 30kV with a probe current of 40 pA and 0.8° grazing angles.

The hardware and software toolkit ASTAR™ from Nanomegas was employed for TEM-ACOM. The interested reader is invited to refer to [44] for additional information. In summary, the region of interest is scanned by a nano-beam. Diffraction patterns are captured using a CCD camera at each scan point. The phase and orientation at each position are determined by post-processing of the diffraction data set, using a template matching technique to compare the experimental diffraction patterns to the theoretical ones of possible phases. It is important to keep in mind that ACOM only builds correlations between acquired and simulated patterns, therefore a preliminary list of possible candidate phases has to be established. Here, the list of the candidate phases was established based on X-ray diffraction investigations and thermodynamic calculations using ThermoCalc. More details can be found in Ref. [45], [46]. The correlation between an experimental diffraction pattern and the theoretical one for a particular phase is measured by the correlation index (I). The best response is given by the simulated pattern showing the highest correlation index. Another index is often used to evaluate the robustness of phase recognition, the phase/orientation reliability index R, which can be written as follows $R = 100(1 - I_1/I_2)$, where I_1 and I_2 are the correlation indices of the two best solutions for the proposed phase and orientation, respectively. When this parameter R is greater than 15 [44], the identified phase is by far the best option among all candidates.

APT specimens were prepared using an FEI Helios Plasma Focused Ion Beam (PFIB) and subsequently analysed on a Cameca Instrument Inc. Local Electrode Atom Probe (LEAP) 5000 XR. The atom probe needle-shaped specimens were run in voltage-pulsing mode, at a base temperature of 40K, with a 20% pulse fraction at a rate of 200 kHz and a 0.5% detection rate. Data analysis was performed using AP Suite 6.1 following a crystallography-based calibration method [36]. The composition of the Al solid solution was extracted from each APT volume by determining the distribution of isolated atoms in the matrix (DIAM algorithm), see [37]. Briefly, the first nearest neighbor distances (1NN) were calculated and extracted from the AP Suite 6.1 software and further calculations were run using Matlab. Regions near grain boundaries or interfaces or intermetallic particles were discarded as such features may influence the results. The probability of finding an isolated atom in a virtual sphere of radius r is calculated and compared to that of a random solid solution. The behavior at larger r is used to extract the matrix composition in the dataset.

2.5. Synchrotron SAXS measurements

The SAXS synchrotron experiments were performed at the French CRG beamline BM02-D2AM at the ESRF. The incident beam energy was chosen to 8keV and the sample-to-detector distance was 0.3 m. The samples were subjected to in-situ heating in a dedicated furnace mounted in the sample environment vacuum vessel, allowing a completely window-less path for the photons. We used the D5 IMXPAD detector. This setup allowed for a q-range of 0.025Å^{-1} - 0.47 Å^{-1}.

The SAXS samples were mechanically ground to a thickness of about 70-100 µm. Only about 12h of in-situ heat-treatment at 400°C in the SAXS were recorded, so that we also measured several ex-situ samples, in particular a sample aged for 96h at 400°C.

The SAXS images were azimuthally integrated, normalized by the incident beam and the sample transmission and thickness, and converted to absolute units with the help of a glassy carbon secondary calibration sample. The resulting I vs q curves were then fitted to a model comprising a Porod-type $1/q^4$ contribution, a constant contribution (corresponding to Laue scattering, remaining fluorescence…), and a contribution of spherical nanoprecipitates which can be attributed to the $L1_2$-Al_3Zr phase.

3. Experimental Results

3.1. Ageing response of the material

Figure 1 plots the hardness over the course of the direct ageing at 400°C after a stress-relief at 300°C/4h, which increases by approximately 20% between the SR conditions (green point, ~130 HV) and the peak-aged condition after 4h at 400°C (orange point, ~155 HV). After 96h at 400°C, the material is overaged but still shows a relatively high hardness, of 120 HV (red point).

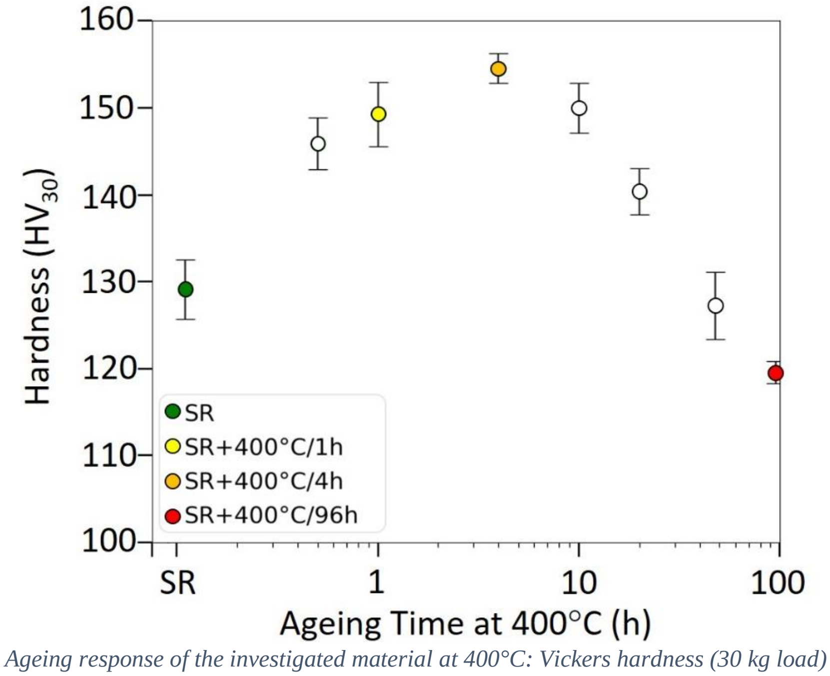

Figure 1 : Ageing response of the investigated material at 400°C: Vickers hardness (30 kg load) vs. ageing time.

3.2. Evolution of the tensile properties

Figure 2a and **Figure 2**b show respectively the engineering and true stress-strain tensile response of the different microstructures of interest, namely SR, SR+400°C/1h, SR+400°C/4h, and SR+400°C/96h. The mechanical properties (yield strength at 0.2% (YS), ultimate tensile strength (UTS), and elongation to failure) are extracted from those curves. Their evolution after ageing at 400°C is shown in **Figure 2**c and **Figure 2**d. The UTS increases during the first hour of ageing at 400°C and then remains constant between 1h and 4h at 400°C. Additionally, the increase in YS occurs mainly during the first hour at 400°C. For the overaged sample (96h at 400°C), the YS decreases to reach a value similar to that of the SR sample. Despite exposure at high temperature for extended periods of time, the overaged (96h) sample maintains a YS (resp. UTS) as high as 300 MPa (resp. 340 MPa). **Figure 2**d indicates a continuous decrease in ductility during ageing at 400°C. The variability in elongation to failure is reflected by the amplitude of the error bars and is attributed to the presence of spatters, see examples in *Figure S 2* in supplementary materials. The decrease in elongation to failure starts to be significant after 4h at 400°C, and finally drops drastically in the overaged sample (400°C/96h). The loss in ductility of the overaged condition can be surprising at a first sight. Indeed, overaging is often a strategy to restore some ductility at the expense of a decrease in YS in precipitation-strengthened Al alloys fabricated by more traditional processing routes and with a limited grain boundary decoration, see e.g. [38]. The large elastoplastic transition and the work-hardening behavior of the different microstructures studied herein are considered outside the scope of the present study. The elastoplastic transition and post-yielding tensile response will be analyzed and discussed in a separate work.

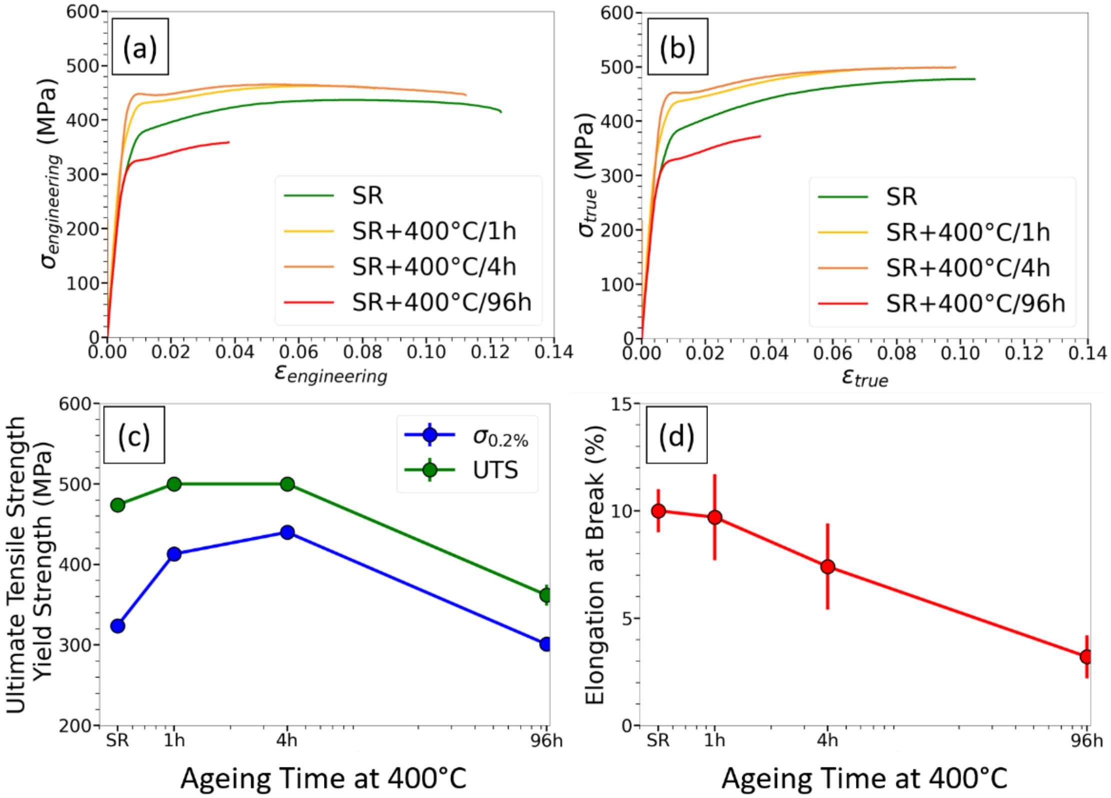

Figure 2 : (a) Engineering and (b) true tensile stress-strain responses of specimens subjected to various heat treatments: SR (in green), SR+400°C/1h (in yellow), SR+400°C/4h (in orange), and SR+400°C/96°C (in red). (c) Evolution of the yield strength taken at 0.2% plastic strain (blue curve), and UTS (green curve) as a function of the ageing time at 400°C. (d) Evolution of the elongation at break with ageing time at 400°C. The standard deviation is represented by the vertical line at each point. A minimum of three specimens per condition were deformed to fracture. The error bars correspond to the minimum and maximum values over the number of tests carried out.

3.3. Evolution of the microstructure at the melt pool scale

Figure 3a is an EBSD-IPF map revealing the typical bimodal grain structure of this alloy in the SR conditions with a fine equiaxed zone (FEZ) at the melt pool boundaries, and the columnar zone (CZ) in the center of the melt pool. No hot cracks were observed, this alloy can thus be considered processable by L-PBF. The fraction of FEZ was estimated by taking the unindexed black regions and by applying a criterion on the sphericity of the indexed grains: grains with a sphericity index < 0.35 are classified as columnar grains (*Figure S 3*). This procedure was applied on at least two low-magnification EBSD maps such as the one shown in **Figure 3**a. The FEZ is found to represent 35 ± 5%, thus the CZ counts for 65 ± 5% of the microstructure. An EBSD-IPF map taken in the FEZ in the SR conditions is given in *Figure S 4a*. The mechanisms responsible for the presence of the FEZ in this alloy have been deeply investigated, see Ref. [34,39,40]. As evidenced in **Figure 3**b for the SR + 400°C/96h sample, the proportion of FEZ and CZ remains relatively stable. Based on **Figure 3**a-b, the grain size in the CZ, taken here as the maximum Feret diameter, is estimated to be approx. 10 μm in both the SR and SR + 400°C/96h. Grain boundary migration or recrystallization are hence limited during direct ageing at 400°C up to 96h (additional maps for 400°C/1h or 400°C/4h are shown in *Figure S 3*-–*Figure S 5*). Complementary SEM observations in the FEZ confirmed that the grain size has only slightly increased after 400°C/96h (*Figure S 4d*).

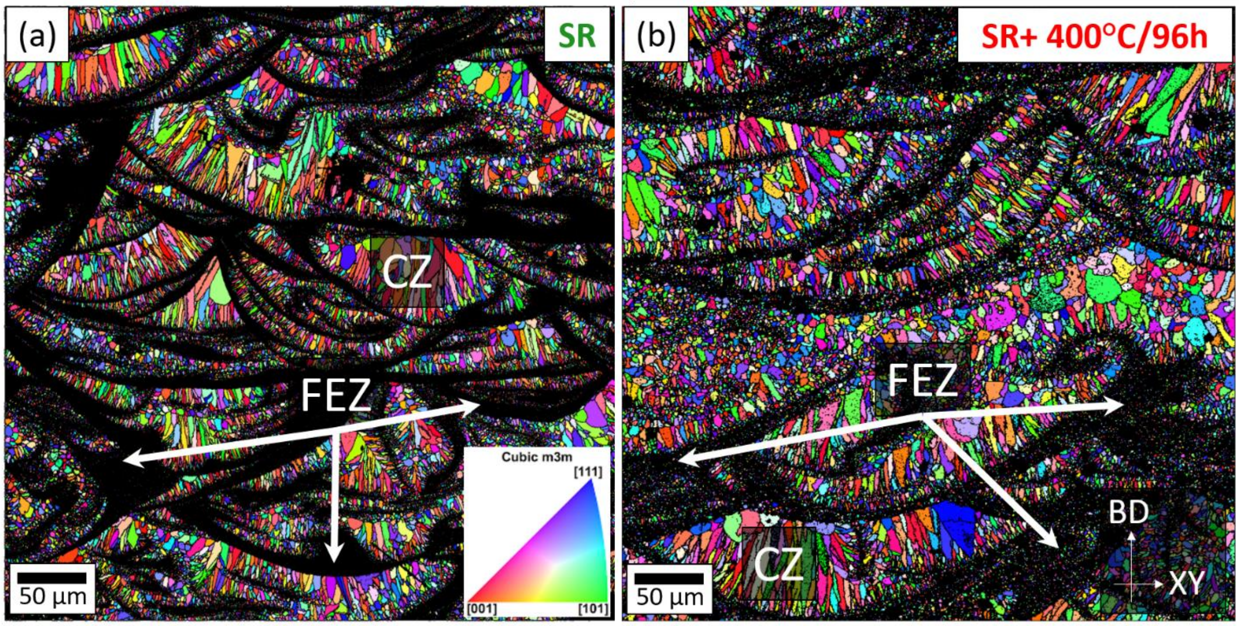

Figure 3: IPF-colour coded EBSD map normal to the Building Direction (BD) in (a) the SR condition, and (b) SR + 400°C/96h revealing the absence of significant variations at the grain scale in both the FEZ and CZ during ageing at 400°C. An EBSD map for each heat-treated sample is shown in Figure S 5.

3.4. Evolution of the intermetallic particles population

The studied alloy contains a substantial concentration of elements with a low solubility in Al, in particular, Ni. The fraction of intermetallic particles was estimated based on image analysis (segmentation) of the images taken using the backscattered electron contrast (BSE), see examples in *Figure S 6*. Intermetallic particles represent 25–30% of the microstructure in the SR conditions.

First, in the FEZ, **Figure 4**a-d (left column) show the evolution of the population of intermetallic particles during ageing at 400°C. In the SR sample, the intermetallic particles are mostly distributed in the intergranular regions in the FEZ, see **Figure 4**a. They exhibit a globular morphology with a size in the range 300–500 nm. In the same region of interest in the SR+400°C/4h sample, only minor evolutions can be evidenced. A slight coarsening of some of the intermetallic particles decorating the grain boundaries is indicated by yellow arrows in **Figure 4**a-c. After 400°C/96h, some intermetallic particles have substantially coarsened, with some showing a flower-like morphology with a size exceeding 10 µm, see e.g. **Figure 4**d. Finally, some pores have nucleated after 400°C/1h, see black regions in **Figure 4**b-c. Further investigations are required to understand the mechanism of pore formation, but this is out of the scope of the present work.

Second, in the CZ**, Figure 4**e-h (right column) show the evolution of the intermetallic particles. **Figure 4**e reveals that, in the SR conditions, the intermetallic particles are slightly finer (<200 nm in width) and exhibit a more elongated morphology in the CZ than in the FEZ. **Figure 4**f shows a substantial modification in the morphology of the intermetallic particles in the SR + 400°C/1h sample. They become more globular in the interdendritic regions, see examples pointed out with yellow arrows in **Figure 4**f-g. Finally, after long-time exposure at 400°C (96h), the intermetallic particles decorating the interdendritic regions have slightly coarsened but remain relatively fine (< 1µm) in comparison with those observed in the FEZ, see **Figure 4**h.

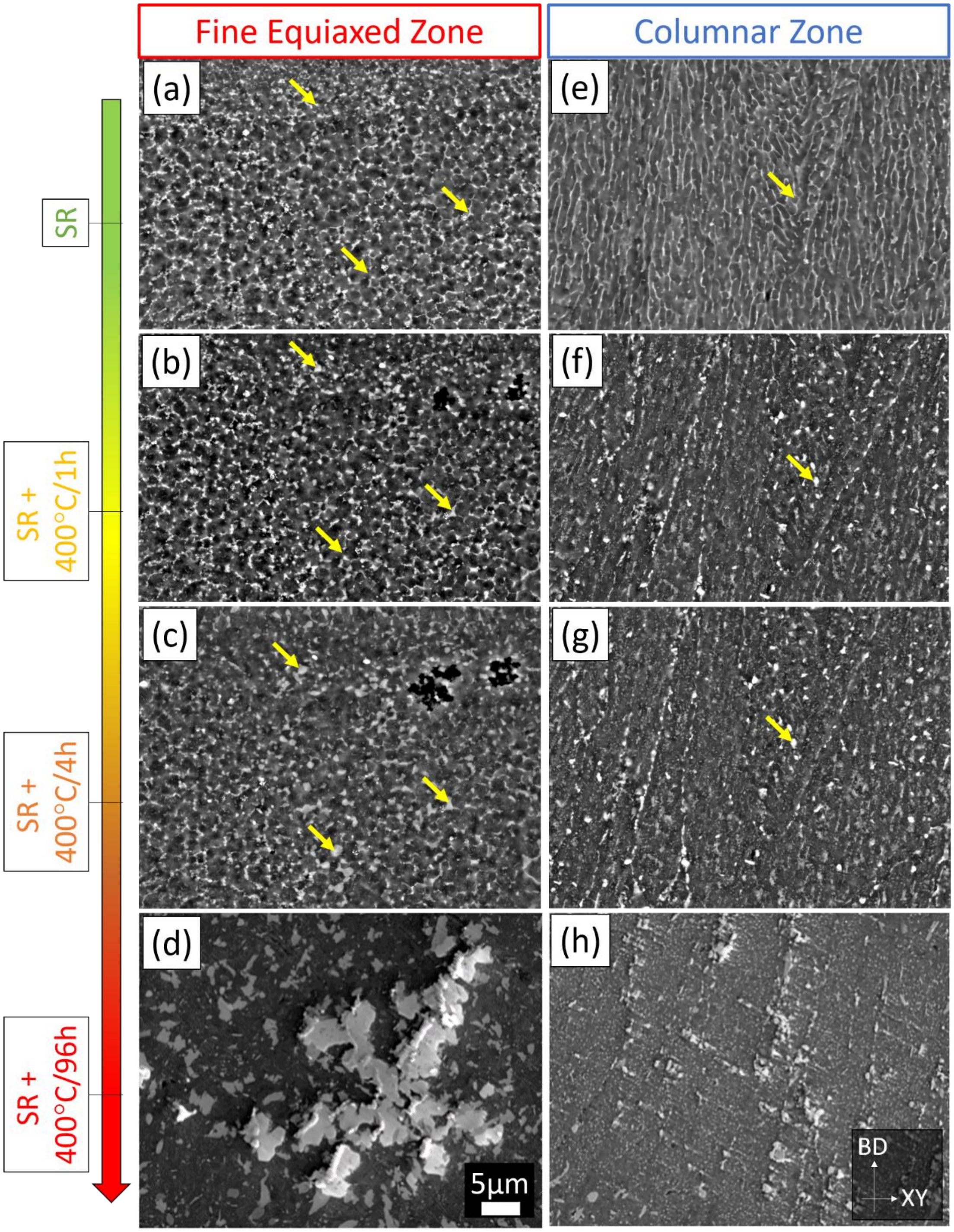

Figure 4: Evolution of the microstructure during direct ageing at 400°C in the FEZ (left) and CZ (right) based on SEM-BSE micrographs :(a-b) SR; (c-d) SR+400°C/1h; (e-f) SR+400°C/4h; (g-h) SR+400°C/96h. To detect slight microstructural evolutions, the same region of interest was observed for the SR, SR+400°C/1h, and SR+400°C/4h. The aluminum matrix appears in dark grey while intermetallic particles show a white contrast.

Elemental partitioning between the matrix and intermetallic particles has been estimated by using EDS mapping in the SEM in both the FEZ and the CZ, see **Figure 5** and **Figure 6**, respectively. The overaged SR+400°C/96h sample was selected for comparison with the SR conditions, since it showed the most significant differences, see **Figure 4**. The EDS maps for the SR+400°C/1h and SR+400°C/4h are provided in supplementary materials, see *Figure S 7* and *Figure S 8* for the FEZ and CZ respectively.

In the FEZ of the SR sample, most of the intermetallic particles are mainly composed of Ni and Cu (**Figure 5**a-c) while some of them contain Mn (**Figure 5**d). At this scale, Zr-rich particles are not detected, see **Figure 5**e. After 400°C/96h, the largest intermetallic particles (>5µm) consist of Ni and Cu, see **Figure 5**f-h. Some of the (Cu, Ni)-rich particles contain more Cu than the others, see **Figure 5**h. Mn-rich micrometer-sized particles in which Ni and Cu also weakly partition can be observed (**Figure 5**i). Zr-rich precipitates can now be distinguished, see **Figure 5**j.

In the CZ of the SR sample, one can only detect Ni and Cu enrichment in the intermetallic particles (**Figure 6**a-c). The spatial resolution of the EDS in the SEM does not allow to reveal Mn or Zr partitioning in the CZ, see **Figure 6**d-e. After 400°C/96h, the largest particles are enriched in Ni and Cu (**Figure 6**f-h) while a few Mn-rich particles containing also Ni and Cu can be observed (**Figure 6**i). Zr-rich particles can hardly be detected (**Figure 6**j).

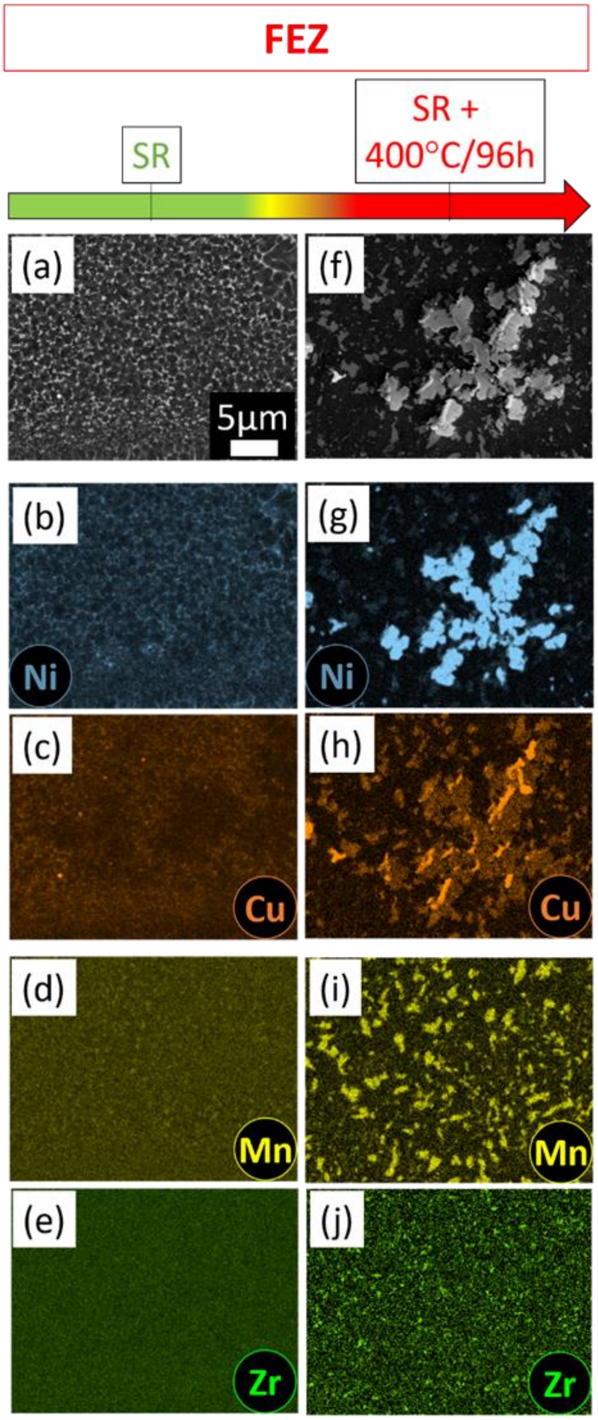

Figure 5 : SEM-EDS chemical analysis of the intermetallic particles observed in the FEZ: (a-e) in the SR sample and (f-j) after SR+400°C/96h. (a) Typical SEM-BSE image of the FEZ after SR, and corresponding (b-e) SEM-EDS maps of Ni, Cu, Mn, and Zr respectively. (f) Typical SEM-BSE image of a FEZ after SR+400°C/96h, and corresponding (g-j) SEM-EDS maps of Ni, Cu, Mn, and Zr respectively.

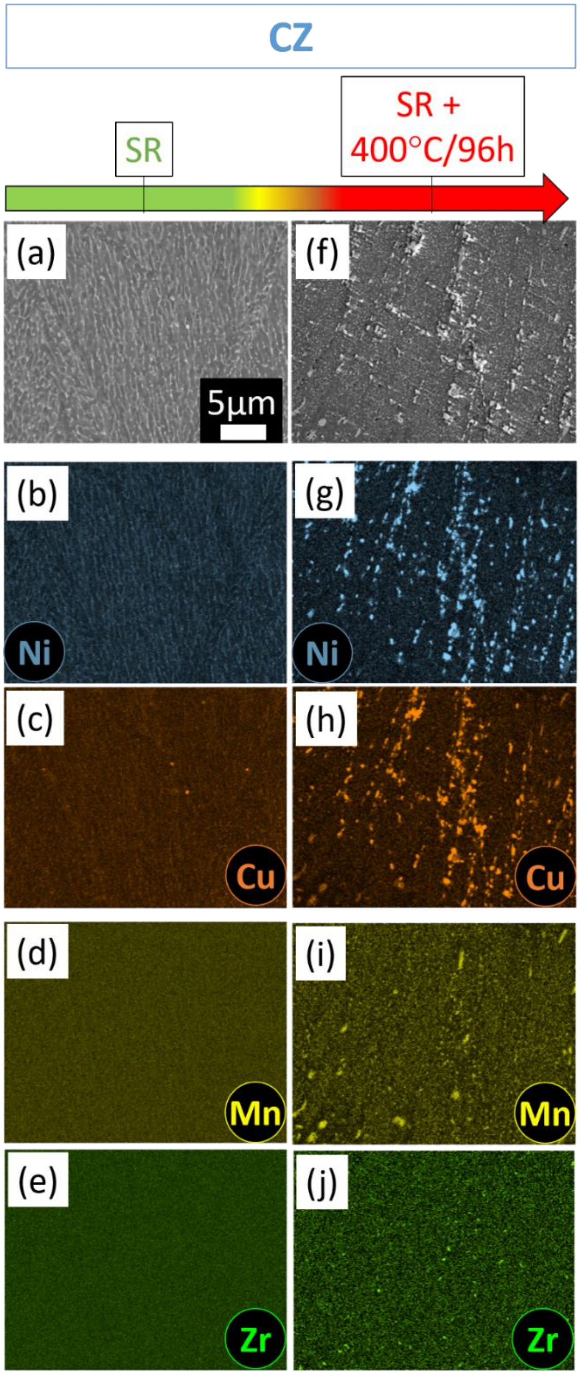

Figure 6 : SEM-EDS chemical analysis of the intermetallic particles observed in the CZ: (a-e) in the SR sample and (f-j) after SR+400°C/96h. (a) Typical SEM-BSE image of the CZ after SR, and corresponding (b-e) SEM-EDS maps of Ni, Cu, Mn, and Zr respectively. (f) Typical SEM-BSE image of a CZ after SR+400°C/96h, and corresponding (g-j) SEM-EDS maps of Ni, Cu, Mn, and Zr respectively.

3.5. Identification of the intermetallic particles using XRD

XRD analyses were used to identify the intermetallic particles, based on the crystallographic information given in the ICCD PDF4 + database. The XRD spectra of the different conditions are given in supplementary materials (*Figure S 9*). **Table 3** summarizes the phases identified in the different samples. The identified phases are referred to using the chemical formula found in the XRD database, although their exact composition may differ as this does not take into account substitution, for instance, the Al_9Ni_2 phase may also contains a significant amount of Cu.

Six phases have been identified in the SR sample, five of them being Al-based intermetallics, which agrees with our previous study in which their presence had been confirmed using nanodiffraction in the TEM, see [39]. Two of the intermetallic phases have a complex structure, namely the Al_9Ni_2 phase (monoclinic) and the $Al_{60}Mn_{11}Ni_4$ phase (orthorhombic). Both show a low symmetry as indicated by the various peaks detected at small angles ($2\theta < 30°$), see *Figure S 9*. The other phases identified are respectively the $L1_2$-Al_3Zr, Al_3Ni_2, and the Al_2Cu phase with cubic, hexagonal, and tetragonal structures respectively. No additional peak has been detected for ageing times below 4h at 400°C (see black, green, and orange spectra in *Figure S 9*). After 400°C/96h, traces of the Al_3Zr-D023 phase are observed (red spectrum in *Figure S 9*).

	Al	**$L1_2$-Al_3Zr**	**$Al_{60}Mn_{11}Ni_4$**	**Al_9Ni_2**	**Al_3Ni_2**	**Al_2Cu**	**D023-Al_3Zr**
SR	⬜	🟩	🟪	🟨	🟦	🟦	X
SR+400°C/1h	⬜	🟩	🟪	🟨	🟦	🟦	X
SR+400°C/4h	⬜	🟩	🟪	🟨	🟦	🟦	X
SR+400°C/96h	⬜	🟩	🟪	🟨	🟦	🟦	🟩

Table 3. Summary of the different the phases identified based on XRD analyses after the various heat treatments investigated. The diffractograms allowing the phase identification are given in supplementary materials, see Figure S 9. Almost all phases are identified in the SR sample. In the SR sample the Al_3Zr phase is cubic ($L1_2$) while its more stable form (hexagonal) Al_3Zr phase (D023) is detected after 96h at 400°C. The details on the crystallographic structure identified are given in Table S 1 in supplementary materials.

3.6. Compositional evolution revealed using APT

The compositional evolution of the solid solution upon ageing is investigate using APT. Examples of APT reconstructions in the SR condition from the FEZ and CZ are shown respectively in **Figure 7**a and **Figure 7**b. **Figure 7**c-d shows examples of APT samples taken in the FEZ and CZ respectively after 1h at 400°C, in which Zr-rich spherical precipitates are revealed by a set of iso-surfaces delineating regions containing over 2.0 at.% Zr. Their composition is close to Al_3Zr, according to composition profiles calculated as a function of the distance to the iso-surfaces as shown in **Figure 7**e and **Figure 7**f.

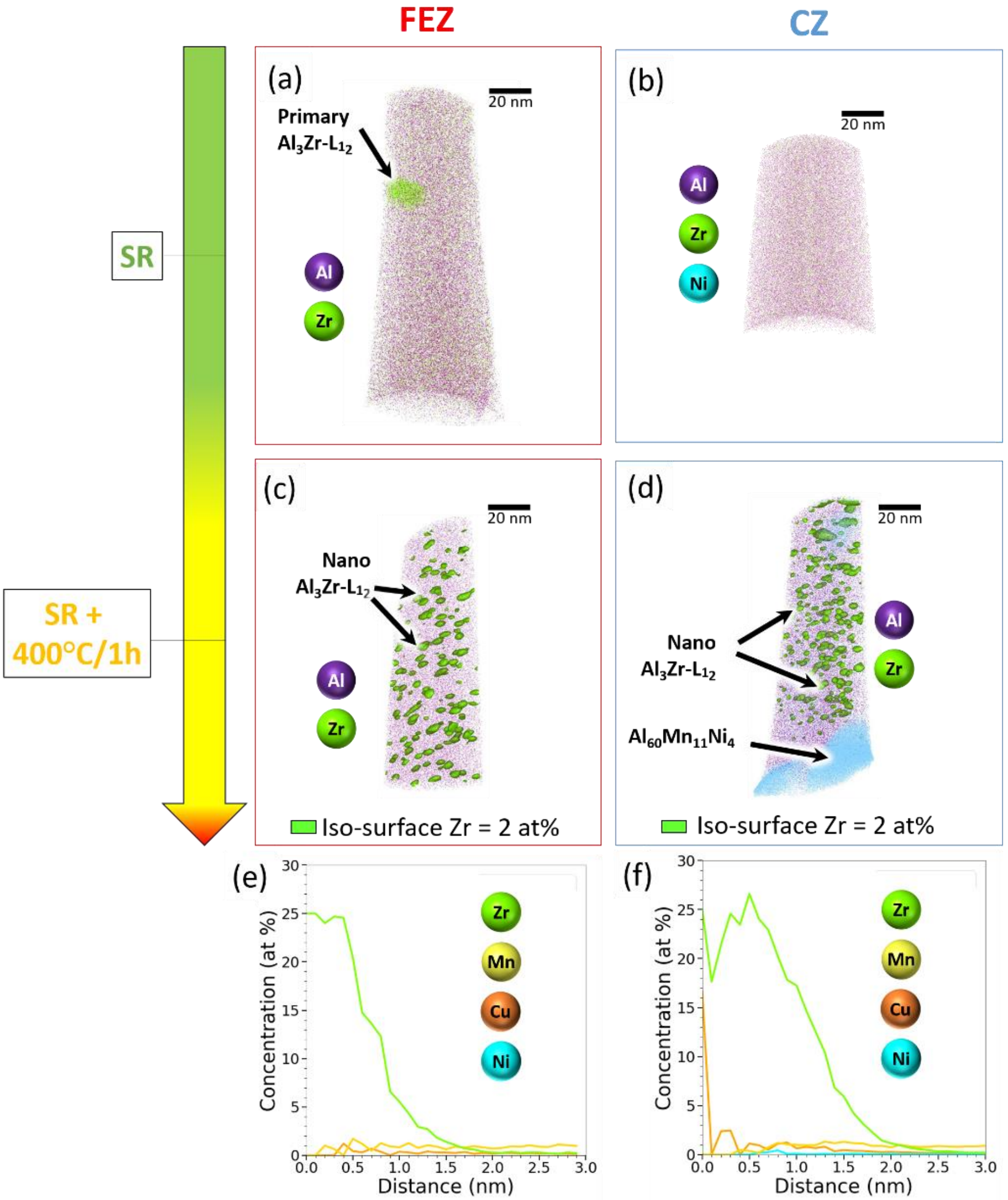

Figure 7 : Examples of 3D APT reconstructions in (a) the FEZ and (b) CZ in the SR conditions indicating the absence of nanoprecipitation; and in (c) the FEZ and (d) CZ of a sample subjected to SR+400°C/1h revealing the presence of spherical nanoprecipitates rich in Zr.(c-d) show examples of 3D atom probe reconstruction in the FEZ and CZ respectively after an additional treatment of 1h at 400°C. Zr-rich spherical nanoprecipitates are revealed with an isosurface of 2.0 at.% Zr and their chemical composition in each zone studied using compositional profiles, examples are given in (e) and (f).

The evolution of the matrix concentration between the SR condition and after ageing at 400°C/1h for Zr, Mn, Cu, and Ni, is given respectively in **Figure 8**a-d. The matrix was analyzed using the methodology proposed in [37]. In the SR condition, the distribution of the distance to the first nearest-neighbor for each solutes is compatible with a random distribution in both FEZ or CZ [41] . This was verified in several APT analyses for each zone. The Zr and Mn contents retained in solid solution in the CZ: Zr = 0.41 at.% and Mn = 1.77 at.% are slightly higher than in the FEZ: Zr = 0.37 at.%, Mn = 1.64 at.%. The Cu content is low, whereas Ni is nearly insoluble in Al.

After aging for 1h at 400°C, the concentration in Zr and Mn have decreased in both regions, and reached respectively 0.20 at.% and 0.7 at.%, see **Figure 8**a-b. Contrary to Zr and Mn, the Cu content in the matrix increases slightly with ageing at 400°C (from ~0.05-0.07 at.% in the SR conditions vs. ~0.15-0.17 at.% after ageing 400°C/1h). Finally, the Ni content does not change upon ageing at 400°C.

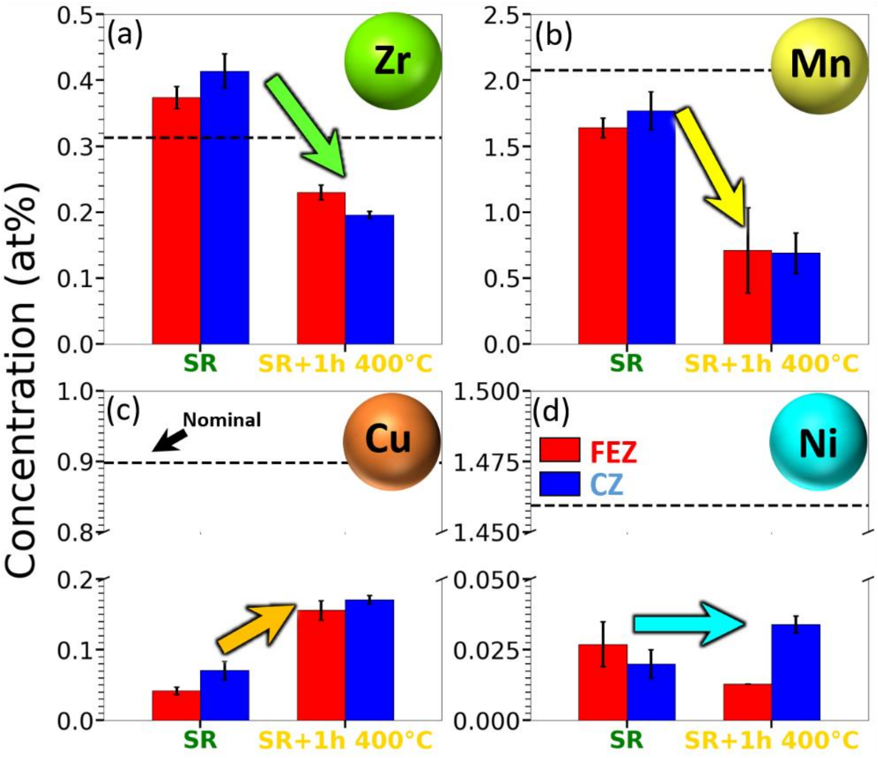

Figure 8 : Composition and evolution of the different solutes retained in the Al solid solution upon ageing at 400°C: (a) Zirconium, (b) Manganese, (c) Copper, and (d) Nickel. Concentration in the FEZ in red, in the CZ in blue. The dashed black lines represent the nominal composition for each alloying element.

Finally, a few coarse particles (between 50 and several hundreds of micrometers) have been detected in APT specimens. Those particles correspond to the intermetallic particles observed in the SEM in **Figure 4**. Their compositions are summarized in **Table 4**. Among the detected particles, most of them contain essentially Cu and Ni, some of them are enriched in Mn but the Zr content within such particles appears rather low. A few Zr-rich particles with a size exceeding 50 nm with a stoichiometry close to the Al_3Zr phase were also found.

Intermetallic particles	Sample (Region)	Zr	Mn	Ni	Cu	Nature
#1	SR (FEZ)	23.96 ± 0.07	0.28 ± 0.64	0.19 ± 0.64	0.90 ± 0.51	Primary Al_3Zr
#2	SR (FEZ)	0.14 ± 0.07	10.94 ± 0.64	10.99 ± 0.64	6.59 ± 0.51	$Al_{60}Mn_{11}Ni_4$
#3	SR (FEZ)	0.28 ± 0.20	0.27 ± 0.19	27.78 ± 1.96	13.94 ± 1.51	Al_3Ni_2
#4	SR (FEZ)	0.27 ± 0.20	6.20 ± 1.56	16.21 ± 2.41	7.76 ± 1.74	Al_9Ni_2
#5	SR (CZ)	0.19 ± 0.15	10.70 ± 1.46	11.07 ± 1.47	5.49 ± 0.99	$Al_{60}Mn_{11}Ni_4$
#6	SR+400°C/1h (FEZ)	0.26 ± 0.20	12.73 ± 1.79	9.87 ± 1.60	2.85 ± 0.89	$Al_{60}Mn_{11}Ni_4$
#7	SR+400°C/1h (CZ)	0.13 ± 0.10	14.24 ± 1.25	7.60 ± 0.95	4.33 ± 0.73	$Al_{60}Mn_{11}Ni_4$
#8	SR+400°C/1h (CZ)	0.11 ± 0.08	12.31 ± 1.45	11.87 ± 1.43	2.11 ± 0.61	$Al_{60}Mn_{11}Ni_4$
#9	SR+400°C/1h (CZ)	0.12 ± 0.12	0.08 ± 0.06	24.69 ± 2.11	16.13 ± 1.78	Al_3Ni_2
#10	SR+400°C/1h (CZ)	0.12 ± 0.09	0.10 ± 0.06	26.4 ± 1.47	16.40 ± 1.23	Al_3Ni_2

Table 4: Summary of the compositions of the intermetallic particles and nanoprecipitates detected in APT reconstructions given in at.%.

3.7. Dual precipitation revealed by TEM

Figure 9a-b and **Figure 9**c-d show TEM analyses carried out respectively in the FEZ and CZ of a SR+400°C/1h sample. The superlattice reflections in the selected area electronic diffraction (SAED) patterns shown in **Figure 9**b and d confirm precipitation of the $L1_2$-Al_3Zr phase in the two zones. This is in agreement with previous reports of Al-alloys containing Zirconium processed by L-PBF, see e.g. [42]. **Figure 9**d reveals a second precipitation in the columnar grains along the [010] direction. The high number of diffraction spots along this direction indicates that the crystal structure has, at least, one large lattice parameter.

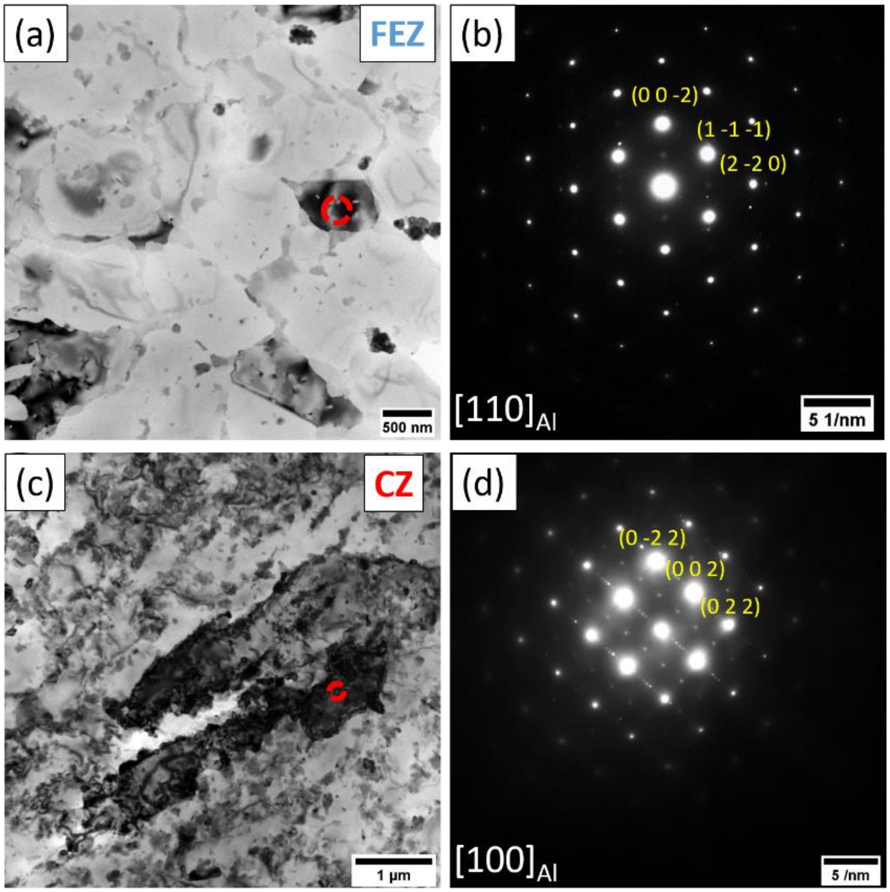

Figure 9: TEM analyses in the SR+400°C/1h sample: (a) BF-TEM image taken in the FEZ and (b)Selected area electronic diffraction pattern from the red circle indicated n (a). (c)BF-TEM image taken in the CZ and (b) SAED pattern from the red circle highlighted in (c).

Further investigations have been carried out by coupling crystallographic information collected using ACOM with chemical information acquired by EDS to study this secondary precipitation. The sub-micron equiaxed grains observed in **Figure 10**a indicates that the analysis was made in the FEZ. The intergranular regions are decorated by relatively coarse intermetallics (>50 nm). Based on the phase recognition provided by ACOM in **Figure 10**a and the EDS maps displayed in **Figure 10**b-e, the $Al_{60}Mn_{11}Ni_4$ phase corresponds to the particles containing Mn, Cu, and Ni while both the Al_9Ni_2 and Al_3Ni_2 phases are associated to the particles enriched in Cu and Ni. The Zr-rich particles are identified as $L1_2$-Al_3Zr. Similar observations can be made in the CZ, see **Figure 10**f-j.

Interestingly, finer intragranular precipitates not observed in the SR sample can be seen in both FEZ and CZ suggesting that they have precipitated during ageing at 400°C. The density of such intragranular precipitates seems higher in the CZ than in the FEZ, see comparison between **Figure 10**a and **Figure 10**f. Those intragranular precipitates rich in Mn, Ni, and Cu have been recognized as the $Al_{60}Mn_{11}Ni_4$ phase, see **Figure 10**a,f. Such precipitates have either a globular (see blue arrows **Figure 10**a) or a plate-like morphology (see white arrows **Figure 10**b).

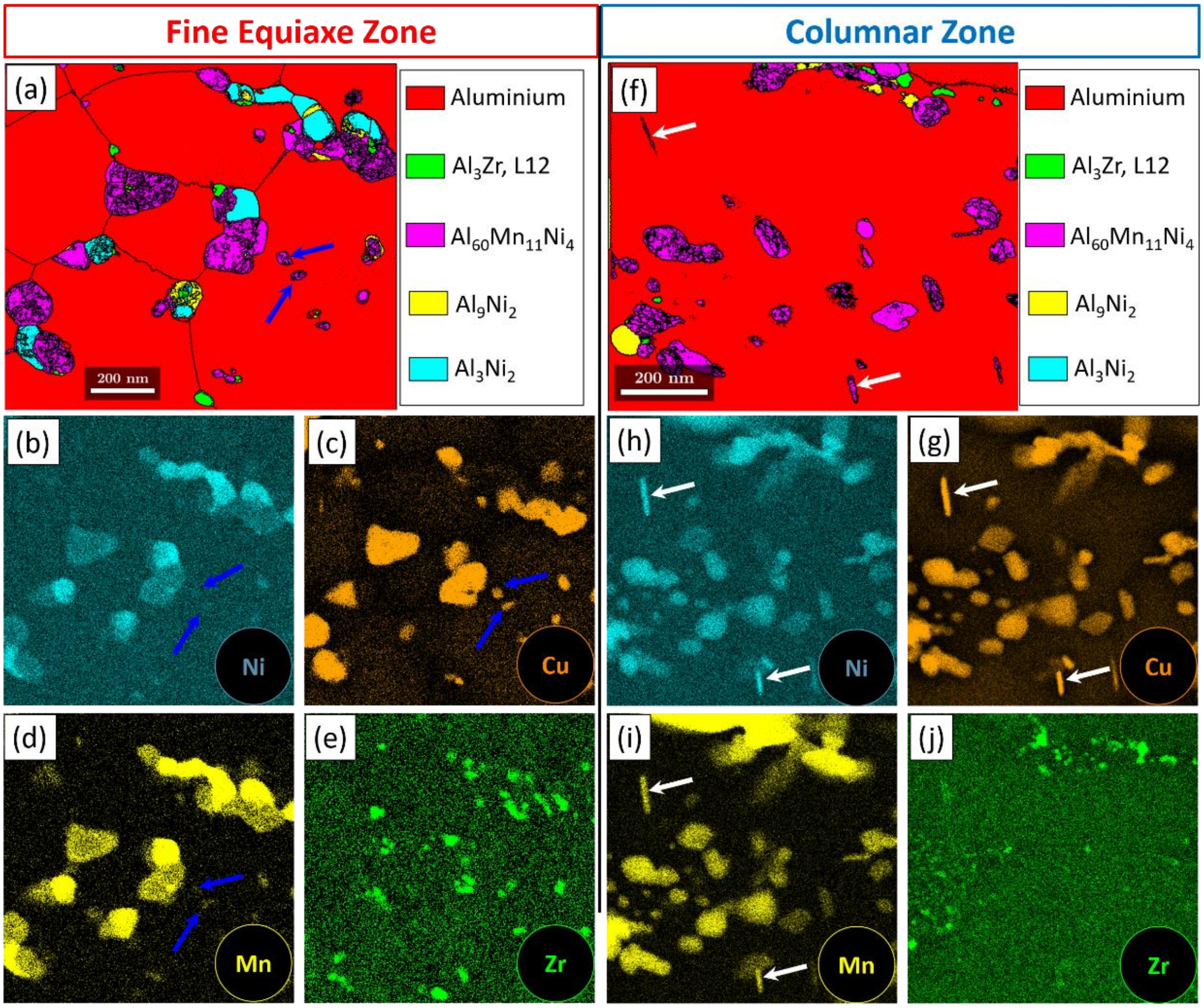

Figure 10 : Study of the secondary nanoprecipitation in the FEZ in a sample subjected to SR+400°C/1h : (a) ACOM – phase map revealing some small precipitates in aluminium grains identified as the $Al_{60}Mn_{11}Ni_4$ complex phase. Elemental EDS maps collected in the same region of interest for: (c) Ni, (b) Cu, (d) Mn, and (e). Study of the secondary nanoprecipitation in the CZ in a sample subjected to SR+400°C/1h: (f) ACOM – phase map revealing some small precipitates in an aluminium grain identified as the $Al_{60}Mn_{11}Ni_4$ x phase. Elemental EDS maps collected in the same region of interest for: (g) Ni, (h) Cu, (i) Mn, and (j) Zr. The Aluminium grains boundaries are represented with black lines. The white (resp. blue) arrows indicate the Mn-rich plate-like (resp. globular) precipitate.

3.7. Monitoring the precipitation kinetics using SAXS

To monitor the precipitation kinetics of the spherical $L1_2$-Al_3Zr nanoprecipitates, in situ and ex situ SAXS measurements were performed during aging at 400°C. The complete in-situ SAXS data set is provided as supplementary materials, see *Figure S 10*. APT analyses provide the precipitate composition necessary to process the SAXS signals. The evolution of both the volume fraction and the radius of the precipitates with the ageing time is shown in **Figure 11**a-b. Ex-situ samples corresponding to the conditions studied in this work were also analyzed and their data are plotted as colored symbols in the same figure. Based on **Figure 11**b, the first stages of precipitation are detected after only 15 min at 400°C. This suggests that the decomposition of the solid solution starts at this point even though the volume fraction of precipitate does not seem to evolve (**Figure 11**). **Figure 11**b reveals that after 1h at 400°C the average radius of the $L1_2$-

Al$_3$Zr nanoprecipitates reaches 1.3 nm in radius which is consistent with the objects identified in the APT experiments using 2 at.% Zr iso-surfaces . The volume fraction of the L1$_2$-Al$_3$Zr nanoprecipitates after 400°C/1h is approximately 0.7%, **Figure 11**a, which agrees with estimates from APT. **Figure 11**a reveals that after 2h at 400°C, the volume fraction reaches its maximum. However, the subsequent decrease may not be meaningful because some of the precipitates may have coarsened to an extent that they are no longer detected and measured by SAXS. The average radius of the nanoprecipitates after 4h at 400°C is in the range of 1.5–1.6 nm.

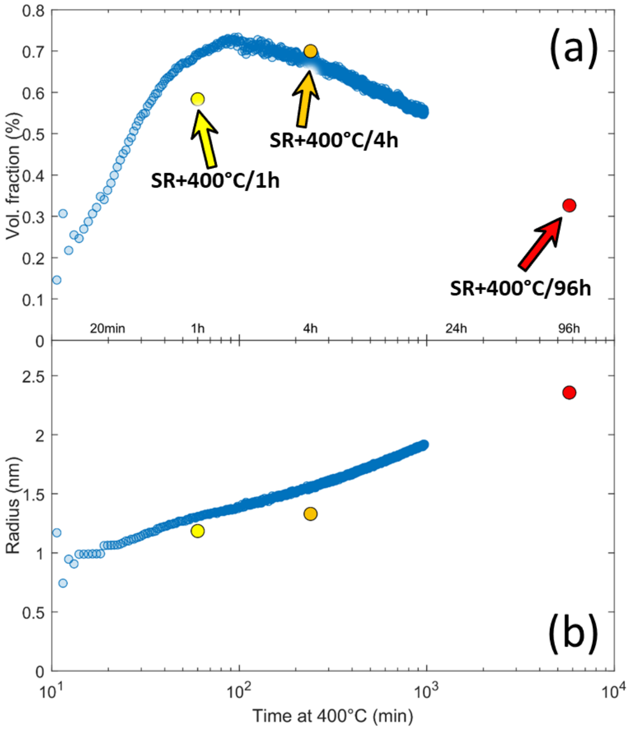

Figure 11 : Evolution of (a) the volume fraction and (b) the radius of the nanoprecipitates with the ageing time at 400°C. The blue curve represents the evolution detected during the in situ test while the yellow, orange, and red symbol stands respectively for the SR+400°C/1h, R+400°C/4h, and SR+400°C/96h conditions that were acquired ex-situ.

4. Discussion

4.1. Classification of the intermetallics population

Correlations between the array of characterization techniques (EDS, XRD, TEM, and APT) used herein enable us to establish a classification of the intermetallic particles observed in this work and whose size exceeds 100 nm. The monoclinic Al_9Ni_2 and hexagonal Al_3Ni_2 structures were detected by XRD (**Table 3**) and their presence was confirmed using ACOM in the TEM (**Figure 10**). Those two phases correspond to the intermetallic particles enriched in Ni and Cu detected in the EDS maps acquired in the SEM suggesting substitution of Ni by Cu. Some intermetallic particles captured in some APT samples (**Table 4**) show a stoichiometry close to those two phases and confirms substitution of Ni by Cu atoms in such intermetallic coumpounds. Thus, those phases should rather be described as $Al_9(Ni,Cu)_2$ and $Al_3(Ni,Cu)_2$. Besides, the flower-like morphology of the largest intermetallic particles observed after 96h at 400°C (**Figure 5**f) is consistent with the six <11-20> principal growth directions contained in the basal plane of the $Al_3(Ni,Cu)_2$ hexagonal structure. The Cu-rich compound observed in **Figure 5**h likely corresponds to the tetragonal structure Al_2Cu detected in the XRD patterns since it is composed exclusively of copper.

The Mn-rich particles detected in **Figure 5**i or in **Figure 6**i are associated with the complex $Al_{60}Mn_{11}Ni_4$ phase. The presence of this phase was also recognized using ACOM in the TEM, see the coarser particles displayed in pink in **Figure 10**a,f. Once again, this intermetallic phase shows traces of substitution because the EDS maps reveal elemental partitioning of Cu in the Mn-rich particles. This was further confirmed by APT because the Mn rich particles contain a non-negligible amount of Cu.

Two forms of the Al_3Zr phase were identified by XRD: the cubic $L1_2$ metastable form found in the SR, SR+400°C/1h, and SR+400°C/4h samples; and the stable D023 form only found in the SR+400°C/96h sample. In the SR conditions, the presence of the metastable $L1_2$ form is associated with the presence of primary $L1_2$-Al_3Zr particles located at the grain center in the FEZ and showing a cubic shape morphology as already shown in [34,39,40]. An example of such a primary $L1_2$-Al_3Zr precipitate was found in the APT sample shown in **Figure 7**a. The Zr-rich particles detected in the EDS maps after long time exposure at 400°C (**Figure 5**j and **Figure 6**j) are thought to be the stable D023-Al_3Zr. Note that the overall fraction of Zr-rich particles can be considered negligible in comparison with the other intermetallic compounds.

The coarsening rate of the intermetallic compounds appears heterogeneous on the melt pool scale since after 400°C/96h, coarser intermetallics are observed in the FEZ compared to the CZ regardless of their nature. Such differences are attributed to the density of interfaces (grain boundaries as well as phase boundaries), which is much higher in the FEZ than in the CZ. Interfaces can be considered fast diffusion paths for solutes, which contribute to increasing the coarsening rate of intermetallics in the FEZ. This idea is supported by complementary APT results showing grain boundary segregation in the FEZ in the SR conditions, especially in Ni and Cu, and Mn, see *Figure S 11*.

Now that the various intermetallic particles have been identified, we propose to classify them into two families depending on their coarsening resistance. Interestingly, the intermetallics that remain fine after 400°C/96h are those enriched in Mn ($Al_{60}Mn_{11}Ni_4$), while those containing mostly Ni and Cu, namely both the $Al_3(Ni,Cu)_2$ and $Al_9(Ni,Cu)_2$ phases, coarsen faster (**Figure 5** and **Figure 6**). The Mn-rich intermetallics can thus be qualified as coarsening resistant. The first explanation is that Mn is a much slower diffuser in Al compared to Ni and Cu. Another factor can be invoked to account for the coarsening resistance of the $Al_{60}Mn_{11}Ni_4$ phase: its crystallographic structure. Indeed, this is a complex phase containing icosahedral building blocks in its unit cell. Such local atomic environments are known to drastically reduce the diffusivity of alloying elements [43–47], even for elements such as Ni or Cu which are usually considered as fast diffusers in Al. One could argue that this idea should also apply to the $Al_9(Ni,Cu)_2$ phase which is also a complex phase. However, we found in the literature that this phase is metastable and may be subjected to a phase transformation leading to the more stable Al_3Ni_2 phase while heating up to 450°C [48]. It is thus assumed here that the $Al_9(Ni,Cu)_2$ would lose its complex nature due to a phase transformation during ageing at 400°C. Then, once transformed into its more stable form $Al_3(Ni,Cu)_2$, its coarsening rate would substantially increases. Deeper investigations would be required to confirm this hypothesis, but the phase maps displayed in **Figure 10**a,f suggest that the Al_3Ni_2 phase is already present in larger proportion than the Al_9Ni_2 phase after SR+400°C/1h though the latter was found in larger proportion in the as-fabricated microstructure, see [34].

4.2. Decomposition of the solid solution and precipitation

In the SR conditions, the analysis of the solid solution using a first nearest-neighbor approach revealed a random distribution of the various solutes. This suggests that the intrinsic heat treatment experienced by the material during the build combined with the SR heat treatment (300°C/4h) do not therefore trigger sufficient diffusion of the slow diffusing Zr and Mn to allow for the formation of clusters or precipitates. The solid solution is supersaturated in Zr and Mn (Zr = 0.37 at.%, Mn = 1.64 at.% in the FEZ and Zr = 0.41 at.% and Mn = 1.77 at.% in the CZ) while Cu and Ni are mostly partitioning in the intermetallic particles, see **Figure 8**. The degree of supersaturation in Zr and Mn can be further appreciated by looking at the maximum solid-state solubility of Zr and Mn in Al based on the Al-Zr and Al-Mn binary systems. Under equilibrium conditions, the maximum solubility of Zr in Al is 0.083 at.% at 660°C [49], while that of Mn in Al is 0.61 at.% at 658°C [50]. Such results suggest that the typical L-PBF processing conditions can be exploited to extend solid-solubility providing new opportunities for enhanced precipitation strengthening. Interestingly, the Zr content retained in the matrix in both the FEZ and CZ is beyond the nominal composition in Zr (0.32 at.%), which can be explained because of the high volume fraction of intermetallic particles (~25-30%) in which Zr substitution is very limited.

Slight differences in matrix composition between the FEZ and CZ in the SR conditions are detected, **Figure 8**. This can be attributed to the higher solid-liquid interface velocity in the CZ which promote solute trapping as suggested in [13,14]. However, the differences appear rather limited. Two factors can be invoked to rationalize this unexpected result. First, it can simply be due to a limited sampling, because the solid-liquid interface velocity is expected to vary locally within a given melt pool. The interface advances faster in the CZ than in the FEZ but local variations can be expected within the CZ: slower interface velocity at the bottom of the CZ and faster at the top. Since APT is a very local characterization technique, it is possible that the specimens were extracted from a region located in the bottom region of a CZ. Second, it has been shown that icosahedral short range order (ISRO) in the liquid during melt pool affects the solidification of this material [39,40]. In particular, the presence of ISRO in the liquid slows down the diffusivity of solutes due to a cage effect, see e.g. Ref. [51,52]. This may contribute to the extension of supersaturated solid solutions at lower liquid-solid interface velocities.

After ageing at 400°C/1h, the decrease in Zr content in the solid solution is associated with the precipitation of $L1_2$-Al_3Zr nanoprecipitates revealed using APT (**Figure 7**c-d) and TEM (**Figure 9**). The decrease in Mn content in the solid solution is attributed to (i) the slight coarsening of the Mn-rich intermetallic coumpounds ($Al_{60}Mn_{11}Ni_4$) already present in the SR conditions and (ii) the precipitation of a Mn-rich phase evidenced by TEM analyses in **Figure 9**d and **Figure 10**. The slight increase in Cu content in the matrix can be attributed to an enhanced solubility of Cu in the Al matrix at 400°C. The Ni content remains unchanged after ageing, indicating that Ni remains essentially trapped in the intermetallic particles.

The overall volume fraction of the $L1_2$-Al_3Zr nanoprecipitates measured by SAXS in the SR+400°C/1h sample was about 0.70%. We verified that this result was in agreement with the APT measurements based on a Zr mass balance in each zone. Both the Zr content in the APT dataset and the Zr content in the matrix are known. Thus, by assuming a Zr content of 23 at.% in the $L1_2$-Al_3Zr nanoprecipitates, we found that the volume fraction was 0.4% in the FEZ and 0.8% in the CZ. Considering now the volume fraction of each zone, this gives an average volume fraction of precipitates of 0.66% which is consistent with the estimation provided by SAXS measurements.

4.3. Ductility loss after 400°C/96h

In traditional precipitation strengthened Al alloys, ductility is restored in the overaging regime, see e.g. [38]. Here, we observed the opposite trend: a loss in ductility in the overaged sample (SR+400°C/96h). The origin of this loss in ductility in the overaged sample can be rationalized by the coarsening of some intermetallics, especially those enriched in Ni and Cu which have been found to coarsen at a much faster rate in comparison to the Mn-rich intermetallics, especially in the FEZ. Although the intermetallic particles show a similar size in the two zones in the SR conditions (**Figure 4**a-b), their evolutions after 96h at 400°C differ significantly. The intermetallics are indeed much coarser in the FEZ than in the CZ after 96h at 400°C, see **Figure 4**g-h. These coarse intermetallics located in the FEZ with a flower-like morphology, containing essentially Ni and Cu (**Figure 5**g), can be easily recognized on the fracture surface of the overaged sample, see *Figure S 12a-b*. A mixed fracture surface can be observed with regions showing dimples (signature of the ductile fracture of the Al matrix) and regions exhibiting a more brittle behavior where fractured flower-like intermetallics can be seen. The fracture occurs hence preferentially in the FEZ due to the presence of these coarse flower like intermetallics (*Figure S 12c-f*). The latter observation suggests that finding ways to prevent the percolation of the FEZ could help to achieve a better ductility after long time exposure at 400°C. More work is needed to evaluate the various strategies to control the respective volume fraction of the FEZ and CZ as well as their 3D arrangement. Such strategies include the effect of preheating, the manipulation of the lasing pattern, as well as the density of inoculating agents (primary $L1_2$-Al_3Zr precipitates).

4.4. Strengthening mechanisms

Hereafter, we discuss the strengthening mechanisms involved in in the FEZ and CZ, which can account for the evolution in the mechanical properties between the SR and SR+400°C/1h states. The objective is to weigh the various contributions and identify which of those contributors are predominant. **Table 5** gives a summary of all the constants used hereafter to estimate the contribution to the yield strength.

Parameters			**References**
σ_0 (MPa)	Friction stress of Al	10	[53]
k_y (MPa.m$^{1/2}$)	Hall Petch parameter	0.07	[54]
M	Taylor factor for a random texture	3.06	
ν	Poisson ratio of Al	0.345	[55]
G_{Al} (GPa)	Shear modulus of Al	25.4	[55]
G_{Al3Zr}	Shear modulus of $L1_2$-Al_3Zr nanoprecipitates	57	[55]
ΔG	Shear modulus mismatch between Al and $L1_2$-Al_3Zr	31.6	
b (nm)	Burgers vector of Al	0.286	[55]
$w = 5b$ (nm)	Interaction force parameter	1.430	
ε_{Mn} (%)	Misfit strain for Mn	-4.20	[56]

ε_{Zr} (%)	Misfit strain for Zr	1.23	[56]
ε_{Ni} (%)	Misfit strain for Ni	-1.94	[56]
ε_{Cu} (%)	Misfit strain for Cu	-3.13	[56]
α	Constant for dislocations strengthening	0.27	[53]
γ_{APB}	Average value of anti-phase boundary	0.445	[55]
α_{Coh}	Constant for coherency strenghtening	2.6	[57]
θ	Constrained lattice parameter mismatch at RT ≈(2/3) δ	0.005	[58]
δ (%)	Lattice parameter misfit between between Al and $L1_2$-Al_3Zr	1	
m	Constant for modulus strengthening	0.85	[57]

Table 5. Summary of all the constants used in this work to estimate the various contributions to the yield strength.

4.4.1. Grain boundary strengthening

Grain boundary strengthening can be estimated using the Hall-Petch relationship $\Delta\sigma_{GB} = k_y d^{-0,5}$ with k_y the Hall-Petch parameter and d the average grain size. Here, the Hall-Petch law was adapted using a rule of mixtures to take into account the presence of both fine equiaxed grains (FEZ) and columnar grains (CZ):

$$\Delta\sigma_{GB} = V_{FEZ} k_y d_{FEZ}^{-0,5} + V_{CZ} k_y d_{CZ}^{-0,5} \tag{1}$$

with V_{FEZ} and V_{CZ} respectively the volume fraction of the FEZ and CZ, and d_{FEZ} and d_{CZ} respectively the average grain size in the EZ and CZ. As no significant variations at the grain scale (proportion of FEZ and CZ as well as grain size in both FEZ and CZ) have been observed when comparing the SR state with the SR+400°C/96h (***Figure S 3***), the contribution of grain boundary strengthening is assumed to be the same in all the microstructures of interest here. There is no consensus in the literature regarding the value of the Hall-Petch parameter k_y in the literature, the latter varying between 0.06-0.07 [54,59] and 0.17 [60]. Thus, taking k_y = 0.07 MPa.m$^{1/2}$ gives a lower bound. With V_{FEZ} = 0.35 and V_{CZ} = 0.65 estimated based on EBSD maps, d_{EZ} = 500 nm and d_{CZ} = 10 µm estimated using the average maximum Feret diameter, the grain boundary strengthening contribution was estimated to be $\Delta\sigma_{GB}$ = 50 MPa ($\Delta\sigma_{GB,FEZ}$ = 35 MPa, $\Delta\sigma_{GB,CZ}$ = 15 MPa) regardless of the microstructure considered. This shows grain boundary strengthening cannot be neglected.

4.4.2. Solid solution strengthening

Contrary to grain boundary strengthening, solid solution strengthening is expected to vary significantly between the SR and SR+ ageing at 400°C as illustrated by **Figure 8** showing the composition of the solid solution in both FEZ and CZ.

Solid-solution strengthening was estimated in each region (FEZ and CZ) from the relation derived by Uesugi et al. [56] from first-principles studies of the lattice constants and lattice distortions caused by different solutes retained in the solid solution in aluminum, see equations (2):

$$\Delta\sigma_{SS} = M\left(\frac{3}{8}\right)^{2/3}\left(\frac{1+\nu}{1-\nu}\right)^{4/3}\left(\frac{w}{b}\right)^{1/3} G \times \sum_i \left|\varepsilon_i\right|^{4/3} c_i^{\,2/3} \tag{2}$$

with M the Taylor factor, ν the Poisson ratio, G the shear modulus of aluminium, b the Burgers vector of FCC Al, w a material parameter called the interaction force range (here we take $w = 5b$ as proposed in [56]), ε_i the misfit strain for the solute i = Mn, Zr, Ni, Cu calculated from the first principles [56] and c_i the concentration of solute i in solid solution. To account for variations in solid solutions between the FEZ and

CZ, we used a simple rule of mixture to provide an estimate of the overall solid solution strengthening as follows:

$$\Delta\sigma_{SS} = V_{FEZ}\Delta\sigma_{SS}^{FEZ} + V_{CZ}\Delta\sigma_{SS}^{CZ} \quad (3)$$

where $\Delta\sigma_{SS}^{FEZ}$ and $\Delta\sigma_{SS}^{CZ}$ are the solid solution strengthening contributions in the FEZ and CZ respectively.

The solid-solution strengthening contributes nearly 200 MPa to the yield strength in the SR but its contribution decreases upon ageing at 400°C/1h and reaches only about 120 MPa, see **Figure 12**. Among the solutes retained in solid solution, Mn is by far the most potent since it brings about 80% of the solid solution contribution.

4.4.3. Dislocations strengthening

Microstructures of Al alloys inherited from casting usually contain a high dislocation density when processed by L-PBF, in particular in the interdendritic regions, see e.g. [61]. Here, our TEM observations do not reveal the same features, most likely because the grain size is much smaller, in the order of the interdendritic spacings (~500-1000 nm). Mehta et al. [62] have estimated the dislocation density using XRD measurements based on the full width at high maxima (FWHM) in a Zr-modified 6061 alloy. Although the FWHM can be also affected by other effects such as atoms in solid solution, they found a dislocation density $\rho_{DIS} = 10^{13}$ m^{-2} in the as-built conditions, and 10^{12} m^{-2} after the T6 heat treatment. The value of $\rho_{DIS} = 10^{13}$ m^{-2} is used here to estimate the dislocation strengthening contribution in the SR conditions although 4h at 300°C can decrease the dislocation density due to recovery effects.

The contribution of dislocation strengthening is then estimated using equation (4).

$$\Delta\sigma_{DIS} = M\alpha Gb\sqrt{\rho_{DIS}} \quad (4)$$

where α is a constant equal to 0.27. In the SR conditions, we found that $\Delta\sigma_{DIS} \approx 20$ MPa. This value is also used for the SR+400°C/1h but should therefore be considered as an upper bound. The main conclusion here is that dislocation strengthening does not seem to contribute greatly to the yield strength, even in SR conditions.

4.4.4. Precipitation strengthening

In its SR state, the microstructure is characterized by a high proportion of relatively coarse intermetallic particles (25-30%) with an average size estimated between 100 nm and 500 nm. Given their size (several hundreds of nanometers) and spatial distribution (most of them are decorating the grain boundaries), such intermetallic particles are expected to provide negligible Orowan looping strengthening. Thus, one can consider that in the SR microstructure, precipitation strengthening is negligible. However, after ageing at 400°C, the formation of the L1$_2$-Al$_3$Zr nanoprecipitates was evidenced using TEM, APT, and SAXS.

The precipitation strengthening brought by the nanoscale precipitates of the L1$_2$-Al$_3$Zr phase can be analyzed by estimating order strengthening $\Delta\sigma_{Ord}$, coherency strengthening $\Delta\sigma_{Coh}$, modulus mismatch strengthening $\Delta\sigma_{Mod}$, and Orowan strengthening $\Delta\sigma_{Oro}$ [23,58]. The equations used to estimate all those contributions can be found in **Appendix A**. Precipitation strengthening ($\Delta\sigma_P$) is then estimated using equation (5):

$$\Delta\sigma_P = \min\left(\Delta\sigma_{Ord}; \left(\Delta\sigma_{Coh} + \Delta\sigma_{Mod}\right); \Delta\sigma_{Oro}\right) \quad (5)$$

We took an average precipitate radius of 1.3 nm and a volume fraction of 0.70%. We think that those values are reasonable given the insights gained from APT and SAXS regarding the size and volume fraction of the nanoprecipitates. Note that because SAXS does not allow the population of nanoprecipitates in the FEZ and CZ to be distinguished, we decided to only provide an overall estimation of the precipitation strengthening contribution. No distinction is made between the FEZ and CZ here. After SR+400°C/1h, it is found that particle strengthening is governed by the coherency and modulus effect and contributes to about nearly $\left(\Delta\sigma_{Coh} + \Delta\sigma_{Mod}\right) \approx 135$ MPa to the yield strength. In those conditions, the nanosized $L1_2$-Al_3Zr are slightly underaged and most likely sheared, in agreement with the literature indicating that the transition between shearing and looping occurs for critical radii > 2.5 nm [55,58].

4.4.5. Weight of the various contributions and estimation of the yield strength

The evolution of the relative weight of the different contributions between the SR and SR+400°C/1h samples are now discussed. In the SR conditions, strengthening predominantly arises from the Hall-Petch effect for about 20%, and solid solution strengthening, which accounts for nearly 70% of the yield strength. After 1h at 400°C, grain boundary strengthening does not change (50 MPa) but represents now only 15% of the yield strength. The solid solution contribution has substantially decreased: 120 vs. 200 MPa in the SR conditions. The main contribution to the yield strength (~135 MPa) is now brought by precipitation strengthening (coherency and modulus) from the nanoscale $L1_2$-Al_3Zr precipitates.

The interactions between different strengthening mechanisms can be complex and various superposition laws have been proposed in the literature [20,22,23]. Here, we assume linear additivity except for dislocation and particle strengthening [53] to provide an estimate of the yield strength, see equation (6).

$$\sigma_y = \sigma_0 + \Delta\sigma_{GB} + \Delta\sigma_{SS} + \sqrt{\Delta\sigma_P^2 + \Delta\sigma_{DIS}^2} \qquad (6)$$

where σ_0 is the friction stress of pure Al (10 MPa). The predictions of the yield strength are summarized in **Figure 12**a. Overall, the predictions of the yield strength from the contributions of the various strengthening mechanisms clearly underestimate the yield strength measured experimentally: 280 (predicted) vs. 320 MPa (measured) for the SR condition, and 320 (predicted) vs. 410 MPa (measured) for the SR+400°C/1h condition. However, one should bear in mind that the microstructure of the material of interest is decorated with a large fraction of intermetallic particles (25-30%), meaning that it can hence be considered as a metal matrix composite reinforced by intermetallic particles. In such materials, it is well known that when the volume fraction of intermetallics exceeds 10%, the material can be strengthened through additional mechanisms. Although this aspect was neglected by various authors investigating Al alloys processed by L-PBF that contain a large fraction of intermetallic particles [20,22], we believe that this aspect deserves to be discussed in more depth.

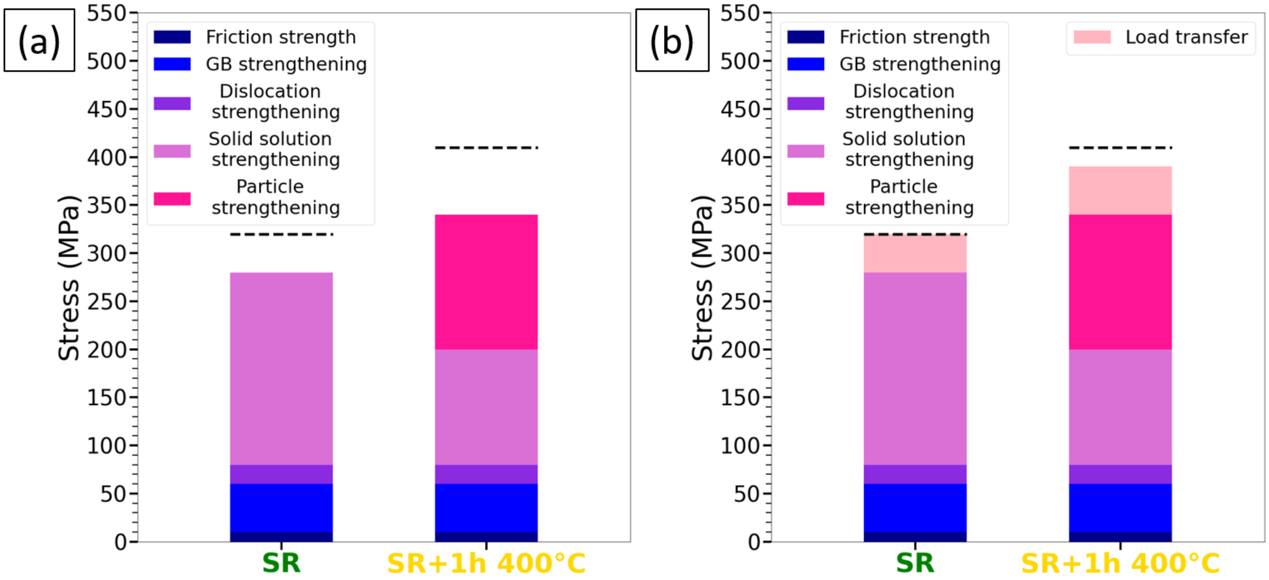

Figure 12 : Summary of the various strengthening contributions to the yield strength in the SR and SR+400°C/1h conditions: (a) without considering the high-volume fraction of intermetallic particles; and (b) by taking into account the role of the high volume fraction of intermetallic particles through a load transfer effect. The material's yield strength measured experimentally from tensile testing are represented using black dashed lines.

4.5. On the role of particle reinforcement

In metal matrix composites, several mechanisms are often invoked to account for their superior strength: (i) load transfer from the soft matrix to the harder reinforcement; (ii) particle strengthening through an Orowan looping mechanism; and (iii) Taylor strengthening due to thermal mismatch (dislocation emission due to differences in coefficient of thermal expansion between the matrix and the intermetallic particles, see e.g. [63–65]. Here, as an attempt to take into account the effect of the reinforcing intermetallic particles, load transfer from the soft matrix to the harder reinforcement is considered. This was done using the simple model proposed by Nardone et Prewo [66] in the 80s for the prediction of the yield strength of aluminum matrix composites reinforced by a discontinuous network of short fibers. We are aware of the limitations of this model in the present case since the reinforcements are not in the form of fibers and are not necessarily aligned with the tensile direction but the objective here was to weigh the role of the high fraction of relatively fine intermetallic particles (< 1 µm). This model relies on a shear-lag model that was modified to take into account tensile load transfer at the end of the fibers. This is particularly important when the reinforcing phase shows a small aspect ratio. The reinforcing phase is assumed to be elastically deformed. The yield strength of the composite is given by equation (7), see [66]:

$$\sigma_{cy} = \sigma_y \left(\frac{1}{2} V_p (s+2) + V_m \right) \qquad (7)$$

where σ_y is the yield strength of the matrix (estimated in section 4.4), V_p , and V_m are respectively the volume fraction of the reinforcing phase and of the matrix, and *s* the aspect ratio of the reinforcing phase. Here, we have considered that the reinforcing phase (intermetallic particles) shows an aspect ratio of *s* = 1. Thus, equation (8) becomes:

$$\sigma_{cy} = \sigma_y \left(\frac{3}{2} V_p + V_m \right). \qquad (8)$$

Taking $V_p = 0.30$, $V_m = 0.70$ and, assuming that those values do not change after 1h at 400°C, it is now possible to provide an estimate of the material's yield strength while including a load transfer effect, see **Figure 12**b. The predictions of the material's yield strength, taking into account the load transfer from the matrix to the intermetallic particles, are now closer to the experimental values. This suggests that the composite nature of the material investigated in this work cannot be neglected. One could argue that the yield strength is still underestimated for the SR+400°C/1h condition but we have to keep in mind that the possible strengthening of the matrix by the Mn-rich nanoprecipitates evidenced in **Figure 9**d and **Figure 10** has been neglected while estimating the weight of the different contributions to the material's yield strength.

5. Summary and conclusions

This article sheds light on the evolution of the microstructure and properties during direct ageing at 400°C of a new Al-4Mn-3Ni-2Cu-1Zr alloy designed for L-PBF based on a multi-scale microstructural study. The main conclusions drawn from the present work can be summarized as follows:

- The investigated alloy is not sensitive to hot cracking and shows a heterogeneous microstructure from the melt pool scale down to the atomic scale.
- In the SR conditions (300°C/4h), this novel alloy exhibits a yield strength of 320 MPa, a UTS of nearly 500 MPa, and an elongation to failure of about 10%. After direct ageing at 400°C/4h (peak-aged conditions), the yield strength reaches 430 MPa, the UTS exceeds 500 MPa, and the elongation at break is about ~7%. After 400°C/96h, the material still shows relatively good mechanical properties with a yield strength above 300 MPa and an elongation to failure slightly lower than 5%.
- At the melt pool scale, fine equiaxed grains (FEZ) with a typical size of roughly 500 nm and representing about ~35% of the microstructure in the SR conditions are found along the melt pool boundaries. Columnar grains (CZ) are found in the melt pool center with a typical width of a few microns. They represent about ~65% of the total grain structure in the SR conditions. The grain structure is found to be nearly unchanged after 96h at 400°C. The presence of relatively fine intermetallics (< 1 μm) decorating the grain boundaries is desirable because it contributes to preventing grain boundary migration and associated mechanisms such as the discontinuous precipitation of the $L1_2$-Al_3Zr phase.
- The microstructure is decorated by a large fraction of relatively fine intermetallic particles, about ~25-30%. Two main families of intermetallic particles have been identified, the ones enriched in Ni and Cu, and those containing Mn in addition to Cu and Ni. During the first four hours at 400°C, the population of intermetallic particles is relatively stable (limited coarsening). For long-time exposure at 400°C, coarsening of the intermetallic particles is observed. The coarsening rate of the particles enriched mostly in Cu and Ni appears to be much faster than that of those containing Mn. The complex $Al_{60}Mn_{11}Ni_4$ phase can thus be qualified coarsening-resistant provided that it is stable up to 400°C and do not lose their complex character.
- At the atomic scale, the matrix solid solution is found to be supersaturated in Mn and Zr in both the FEZ and CZ but to a greater extent in the CZ even after 300°C/4h (SR) with no detectable cluster/precipitates. Ni and Cu are present in minor quantities in the matrix solid solution since they are trapped in the intermetallic particles. At 400°C, the solid solution starts to decompose and the peak-age is achieved at 400°C/4h. Two nanoscale precipitates have been identified using TEM and APT: spherical $L1_2$-Al_3Zr and needle-like $Al_{60}Mn_{11}Ni_4$, the latter showing a much lower volume fraction.

- The kinetics of the formation of the spherical $L1_2$-Al_3Zr nanoprecipitates was monitored using SAXS using synchrotron radiation. Precipitation starts after only 15 minutes at 400°C, and after 1h at 400°C the volume fraction of precipitates was estimated to be ~0.75% with an average radius of 1.5 nm.
- In the SR conditions, the yield strength is dominated by grain boundary strengthening and, to a greater extent, solid solution strengthening, thanks to a very high content of Mn retained in solid solution (> 1.5 at.%). After 400°C/1h, the yield strength results from the superposition of various mechanisms but particle strengthening becomes the most important contribution.
- Yield strength predictions taking into account the contribution of the various strengthening mechanisms (grain boundary strengthening, solid solution strengthening, precipitation strengthening and dislocations strengthening) systematically underestimate the alloy's yield strength in comparison with the experimental results. This means that the role of the large fraction of intermetallic particles cannot be neglected. A simple modified shear lag model was used to take into account load transfer from the matrix to the intermetallic particles. This simple model gives the right order of magnitude for the material's yield strength.

Declaration of Competing Interest

The authors declare that they have no known competing financial interests or personal relationships that could have appeared to influence the work reported in this paper.

Acknowledgements

The authors are grateful to the AEROPRINT project supported by the Région Rhône-Alpes Auvergne. This work has benefited from the characterization equipment of the Grenoble INP CMTC platform supported by the Centre of Excellence of Multifunctional Architectured Materials "CEMAM" n◦ANR-10-LABX-44-01 funded by the Investments for the Future program. The SAXS experiment was performed at the French CRG beamline BM02-D2AM at the European Synchrotron Radiation Facility (ESRF) during experiment IH-HC-3595. The assistance of Dr G. Chahine, Dr N. Blanc and S. Arnaud is gratefully acknowledged. Maxence Buttard acknowledges the Max-Planck-Institut für Eisenforschung GmbH for the financial support offered in the framework of the Coffee Max Planck awards. Martí López Freixes acknowledges the financial support from Constellium SE.

References

[1] A. du Plessis, S.M.J. Razavi, M. Benedetti, S. Murchio, M. Leary, M. Watson, D. Bhate, F. Berto, Properties and applications of additively manufactured metallic cellular materials: A review, Progress in Materials Science. 125 (2022) 100918. https://doi.org/10.1016/j.pmatsci.2021.100918.

[2] L.-Y. Chen, S.-X. Liang, Y. Liu, L.-C. Zhang, Additive manufacturing of metallic lattice structures: Unconstrained design, accurate fabrication, fascinated performances, and challenges, Materials Science and Engineering: R: Reports. 146 (2021) 100648. https://doi.org/10.1016/j.mser.2021.100648.

[3] G. Del Guercio, D.G. McCartney, N.T. Aboulkhair, S. Robertson, R. Maclachlan, C. Tuck, M. Simonelli, Cracking behaviour of high-strength AA2024 aluminium alloy produced by Laser Powder Bed Fusion, Additive Manufacturing. 54 (2022) 102776. https://doi.org/10.1016/j.addma.2022.102776.

[4] A. Sonawane, G. Roux, J.-J. Blandin, A. Despres, G. Martin, Cracking mechanism and its sensitivity to processing conditions during laser powder bed fusion of a structural Aluminum alloy., Materialia. (2020) 100976. https://doi.org/10.1016/j.mtla.2020.100976.

[5] J.H. Martin, B.D. Yahata, J.M. Hundley, J.A. Mayer, T.A. Schaedler, T.M. Pollock, 3D printing of high-strength aluminium alloys, Nature. 549 (2017) 365–369. https://doi.org/10.1038/nature23894.

[6] S.Z. Uddin, L.E. Murr, C.A. Terrazas, P. Morton, D.A. Roberson, R.B. Wicker, Processing and characterization of crack-free aluminum 6061 using high-temperature heating in laser powder bed fusion additive manufacturing, Additive Manufacturing. 22 (2018) 405–415. https://doi.org/10.1016/j.addma.2018.05.047.

[7] P. Mair, L. Kaserer, J. Braun, N. Weinberger, I. Letofsky-Papst, G. Leichtfried, Microstructure and mechanical properties of a TiB2-modified Al–Cu alloy processed by laser powder-bed fusion, Materials Science and Engineering: A. 799 (2021) 140209. https://doi.org/10.1016/j.msea.2020.140209.

[8] P. Mair, V.S. Goettgens, T. Rainer, N. Weinberger, I. Letofsky-Papst, S. Mitsche, G. Leichtfried, Laser powder bed fusion of nano-CaB6 decorated 2024 aluminum alloy, Journal of Alloys and Compounds. 863 (2021) 158714. https://doi.org/10.1016/j.jallcom.2021.158714.

[9] C. Galera-Rueda, M.L. Montero-Sistiaga, K. Vanmeensel, M. Godino-Martínez, J. Llorca, M.T. Pérez-Prado, Icosahedral quasicrystal-enhanced nucleation in Al alloys fabricated by selective laser melting, Additive Manufacturing. 44 (2021) 102053. https://doi.org/10.1016/j.addma.2021.102053.

[10] M. Opprecht, J.-P. Garandet, G. Roux, C. Flament, M. Soulier, A solution to the hot cracking problem for aluminium alloys manufactured by laser beam melting, Acta Materialia. 197 (2020) 40–53. https://doi.org/10.1016/j.actamat.2020.07.015.

[11] M. Opprecht, J.-P. Garandet, G. Roux, C. Flament, An understanding of duplex microstructures encountered during high strength aluminium alloy laser beam melting processing, Acta Materialia. 215 (2021) 117024. https://doi.org/10.1016/j.actamat.2021.117024.

[12] M. Schuster, A. De Luca, A. Mathur, E. Hosseini, C. Leinenbach, Precipitation in a 2xxx series Al-Cu-Mg-Zr alloy fabricated by laser powder bed fusion, Materials & Design. 211 (2021) 110131. https://doi.org/10.1016/j.matdes.2021.110131.

[13] J.R. Croteau, S. Griffiths, M.D. Rossell, C. Leinenbach, C. Kenel, V. Jansen, D.N. Seidman, D.C. Dunand, N.Q. Vo, Microstructure and mechanical properties of Al-Mg-Zr alloys processed by selective laser melting, Acta Materialia. 153 (2018) 35–44. https://doi.org/10.1016/j.actamat.2018.04.053.

[14] S. Griffiths, M.D. Rossell, J. Croteau, N.Q. Vo, D.C. Dunand, C. Leinenbach, Effect of laser rescanning on the grain microstructure of a selective laser melted Al-Mg-Zr alloy, Materials Characterization. 143 (2018) 34–42. https://doi.org/10.1016/j.matchar.2018.03.033.

[15] F. Xiao, S. Wang, Y. Wang, D. Shu, G. Zhu, B. Sun, D. StJohn, Niobium nanoparticle-enabled grain refinement of a crack-free high strength Al-Zn-Mg-Cu alloy manufactured by selective laser

melting, Journal of Alloys and Compounds. 900 (2022) 163427. https://doi.org/10.1016/j.jallcom.2021.163427.

[16] F. Leijon, S. Wachter, Z. Fu, C. Körner, S. Skjervold, J. Moverare, A novel rapid alloy development method towards powder bed additive manufacturing, demonstrated for binary Al-Ti, -Zr and -Nb alloys, Materials & Design. 211 (2021) 110129. https://doi.org/10.1016/j.matdes.2021.110129.

[17] J.H. Martin, B. Yahata, J. Mayer, R. Mone, E. Stonkevitch, J. Miller, M.R. O'Masta, T. Schaedler, J. Hundley, P. Callahan, T. Pollock, Grain refinement mechanisms in additively manufactured nano-functionalized aluminum, Acta Materialia. 200 (2020) 1022–1037. https://doi.org/10.1016/j.actamat.2020.09.043.

[18] M. Roscher, S. Balachandran, D. Mayweg, E. Jägle, Development of Al-Ti-based alloys for laser powder bed fusion, Additive Manufacturing. 47 (2021) 102315. https://doi.org/10.1016/j.addma.2021.102315.

[19] J. Zhang, J. Gao, B. Song, L. Zhang, C. Han, C. Cai, K. Zhou, Y. Shi, A novel crack-free Ti-modified Al-Cu-Mg alloy designed for selective laser melting, Additive Manufacturing. 38 (2021) 101829. https://doi.org/10.1016/j.addma.2020.101829.

[20] Z. Zhu, F.L. Ng, H.L. Seet, W. Lu, C.H. Liebscher, Z. Rao, D. Raabe, S. Mui Ling Nai, Superior mechanical properties of a selective-laser-melted AlZnMgCuScZr alloy enabled by a tunable hierarchical microstructure and dual-nanoprecipitation, Materials Today. 52 (2022) 90–101. https://doi.org/10.1016/j.mattod.2021.11.019.

[21] Q. Jia, P. Rometsch, P. Kürnsteiner, Q. Chao, A. Huang, M. Weyland, L. Bourgeois, X. Wu, Selective laser melting of a high strength AlMnSc alloy: Alloy design and strengthening mechanisms, Acta Materialia. 171 (2019) 108–118. https://doi.org/10.1016/j.actamat.2019.04.014.

[22] D. Bayoumy, K. Kwak, T. Boll, S. Dietrich, D. Schliephake, J. Huang, J. Yi, K. Takashima, X. Wu, Y. Zhu, A. Huang, Origin of non-uniform plasticity in a high-strength Al-Mn-Sc based alloy produced by laser powder bed fusion, Journal of Materials Science & Technology. 103 (2022) 121–133. https://doi.org/10.1016/j.jmst.2021.06.042.

[23] R. Li, M. Wang, Z. Li, P. Cao, T. Yuan, H. Zhu, Developing a high-strength Al-Mg-Si-Sc-Zr alloy for selective laser melting: Crack-inhibiting and multiple strengthening mechanisms, Acta Materialia. 193 (2020) 83–98. https://doi.org/10.1016/j.actamat.2020.03.060.

[24] C. Pauzon, M. Buttard, A. Després, B. Chehab, J.-J. Blandin, G. Martin, A novel laser powder bed fusion Al-Fe-Zr alloy for superior strength-conductivity trade-off, Scripta Materialia. 219 (2022) 114878. https://doi.org/10.1016/j.scriptamat.2022.114878.

[25] M. Genc, P. Eloi, J.-J. Blandin, C. Pascal, P. Donnadieu, F. De Geuser, P. Lhuissier, C. Desrayaud, G. Martin, Optimization of the strength vs. conductivity trade-off in an aluminium alloy designed for laser powder bed fusion, Materials Science and Engineering: A. 858 (2022) 144139. https://doi.org/10.1016/j.msea.2022.144139.

[26] R.A. Michi, A. Plotkowski, A. Shyam, R.R. Dehoff, S.S. Babu, Towards high-temperature applications of aluminium alloys enabled by additive manufacturing, International Materials Reviews. 67 (2022) 298–345. https://doi.org/10.1080/09506608.2021.1951580.

[27] R.A. Michi, K. Sisco, S. Bahl, Y. Yang, J.D. Poplawsky, L.F. Allard, R.R. Dehoff, A. Plotkowski, A. Shyam, A creep-resistant additively manufactured Al-Ce-Ni-Mn alloy, Acta Materialia. 227 (2022) 117699. https://doi.org/10.1016/j.actamat.2022.117699.

[28] A. Plotkowski, K. Sisco, S. Bahl, A. Shyam, Y. Yang, L. Allard, P. Nandwana, A.M. Rossy, R.R. Dehoff, Microstructure and properties of a high temperature Al–Ce–Mn alloy produced by additive manufacturing, Acta Materialia. 196 (2020) 595–608. https://doi.org/10.1016/j.actamat.2020.07.014.

[29] A. Plotkowski, O. Rios, N. Sridharan, Z. Sims, K. Unocic, R.T. Ott, R.R. Dehoff, S.S. Babu, Evaluation of an Al-Ce alloy for laser additive manufacturing, Acta Materialia. 126 (2017) 507–519. https://doi.org/10.1016/j.actamat.2016.12.065.

[30] H. Hyer, A. Mehta, K. Graydon, N. Kljestan, M. Knezevic, D. Weiss, B. McWilliams, K. Cho, Y. Sohn, High strength aluminum-cerium alloy processed by laser powder bed fusion, Additive Manufacturing. 52 (2022) 102657. https://doi.org/10.1016/j.addma.2022.102657.

[31] M. Hesselmann, D. Knoop, J. Epp, V. Uhlenwinkel, A. von Hehl, A. Toenjes, Effect of precipitation-forming elements in a near-eutectic Al-Ce alloy for Laser Powder Bed Fusion, Additive Manufacturing. 57 (2022) 102959. https://doi.org/10.1016/j.addma.2022.102959.

[32] H. Lv, P. Peng, T. Feng, H. Gao, J. Ju, B. Wang, J. Wang, B. Sun, High-performance co-continuous Al-Ce-Mg alloy with in-situ nano-network structure fabricated by laser powder bed fusion, Additive Manufacturing. 60 (2022) 103218. https://doi.org/10.1016/j.addma.2022.103218.

[33] M.T. Pérez-Prado, A. Martin, D.F. Shi, S. Milenkovic, C.M. Cepeda-Jiménez, An Al-5Fe-6Cr alloy with outstanding high temperature mechanical behavior by laser powder bed fusion, Additive Manufacturing. 55 (2022) 102828. https://doi.org/10.1016/j.addma.2022.102828.

[34] M. Buttard, B. Chehab, R. Shahani, F. Robaut, G. Renou, C. Tassin, E. Rauch, P. Donnadieu, A. Deschamps, J.-J. Blandin, G. Martin, Multi-scale microstuctural investigation of a new Al-Mn-Ni-Cu-Zr aluminium alloy processed by laser powder bed fusion, Materialia. 18 (2021) 101160. https://doi.org/10.1016/j.mtla.2021.101160.

[35] Q. Li, G. Li, X. Lin, D. Zhu, J. Jiang, S. Shi, F. Liu, W. Huang, K. Vanmeensel, Development of a high strength Zr/Sc/Hf-modified Al-Mn-Mg alloy using Laser Powder Bed Fusion: Design of a heterogeneous microstructure incorporating synergistic multiple strengthening mechanisms, Additive Manufacturing. 57 (2022) 102967. https://doi.org/10.1016/j.addma.2022.102967.

[36] B. Gault, M.P. Moody, F. De Geuser, G. Tsafnat, A. La Fontaine, L.T. Stephenson, D. Haley, S.P. Ringer, Advances in the calibration of atom probe tomographic reconstruction, Journal of Applied Physics. 105 (2009) 034913. https://doi.org/10.1063/1.3068197.

[37] F.De Geuser, W. Lefebvre, Determination of matrix composition based on solute-solute nearest-neighbor distances in atom probe tomography, Microscopy Research and Technique. 74 (2011) 257–263. https://doi.org/10.1002/jemt.20899.

[38] G. Fribourg, Y. Bréchet, A. Deschamps, A. Simar, Microstructure-based modelling of isotropic and kinematic strain hardening in a precipitation-hardened aluminium alloy, Acta Materialia. 59 (2011) 3621–3635. https://doi.org/10.1016/j.actamat.2011.02.035.

[39] M. Buttard, G. Martin, X. Bataillon, G. Renou, P. Lhuissier, J. Vilanova, B. Chehab, P. Jarry, J.-J. Blandin, P. Donnadieu, Towards an alloy design strategy by tuning liquid local ordering: what solidification of an Al-alloy designed for laser powder bed fusion teaches us, Additive Manufacturing. (2022) 103313. https://doi.org/10.1016/j.addma.2022.103313.

[40] M. Buttard, G. Martin, P. Harrison, E.F. Rauch, B. Chéhab, P. Jarry, J.-J. Blandin, P. Donnadieu, Evidence that the liquid structure affects the nucleation of the primary metastable L12-Al3Zr in additive manufacturing, Scripta Materialia. 226 (2023) 115212. https://doi.org/10.1016/j.scriptamat.2022.115212.

[41] L.T. Stephenson, M.P. Moody, P.V. Liddicoat, S.P. Ringer, New Techniques for the Analysis of Fine-Scaled Clustering Phenomena within Atom Probe Tomography (APT) Data, Microscopy and Microanalysis. 13 (2007) 448–463. https://doi.org/10.1017/S1431927607070900.

[42] Q. Jia, F. Zhang, P. Rometsch, J. Li, J. Mata, M. Weyland, L. Bourgeois, M. Sui, X. Wu, Precipitation kinetics, microstructure evolution and mechanical behavior of a developed Al–Mn–Sc alloy fabricated by selective laser melting, Acta Materialia. 193 (2020) 239–251. https://doi.org/10.1016/j.actamat.2020.04.015.

[43] R. Galler, H. Mehrer, Diffusion in icosahedral Al–Pd–Mn quasicrystals: temperature and pressure dependence, Materials Science and Engineering: A. 294–296 (2000) 693–696. https://doi.org/10.1016/S0921-5093(00)01145-X.

[44] Chr. Khoukaz, R. Galler, H. Mehrer, P.C. Canfield, I.R. Fisher, M. Feuerbacher, Diffusion of 57Co in decagonal Al–Ni–Co-quasicrystals, Materials Science and Engineering: A. 294–296 (2000) 697–701. https://doi.org/10.1016/S0921-5093(00)01149-7.

[45] H.-E. Schaefer, F. Baier, M.A. Müller, K.J. Reichle, K. Reimann, A.A. Rempel, K. Sato, F. Ye, X. Zhang, W. Sprengel, Vacancies and atomic processes in intermetallics – From crystals to quasicrystals and bulk metallic glasses, Physica Status Solidi (b). 248 (2011) 2290–2299. https://doi.org/10.1002/pssb.201147103.

[46] M. Denkinger, H. Mehrer, Diffusion in the C15-type intermetallic Laves phase NbCo2, Philosophical Magazine A. 80 (2000) 1245–1263. https://doi.org/10.1080/01418610008212113.
[47] H. Mehrer, Diffusion in Intermetallics, Materials Transactions, JIM. 37 (1996) 1259–1280. https://doi.org/10.2320/matertrans1989.37.1259.
[48] A. Ustinov, S. Demchenkov, Influence of metastable Al9Ni2 phase on the sequence of phase transformations initiated by heating of Al/Ni multilayer foils produced by EBPVD method, Intermetallics. 84 (2017) 82–91.
[49] K.E. Knipling, D.C. Dunand, D.N. Seidman, Nucleation and Precipitation Strengthening in Dilute Al-Ti and Al-Zr Alloys, Metall Mater Trans A. 38 (2007) 2552–2563. https://doi.org/10.1007/s11661-007-9283-6.
[50] M. Asgar-Khan, M. Medraj, Thermodynamic Description of the Mg-Mn, Al-Mn and Mg-Al-Mn Systems Using the Modified Quasichemical Model for the Liquid Phases, Materials Transactions. 50 (2009) 1113–1122. https://doi.org/10.2320/matertrans.MRA2008484.
[51] G. Kurtuldu, P. Jarry, M. Rappaz, Influence of icosahedral short range order on diffusion in liquids: A study on Al-Zn-Cr alloys, Acta Materialia. 115 (2016) 423–433. https://doi.org/10.1016/j.actamat.2016.05.051.
[52] A. Pasturel, N. Jakse, Influence of Cr on local order and dynamic properties of liquid and undercooled Al–Zn alloys, J. Chem. Phys. 146 (2017) 184502. https://doi.org/10.1063/1.4982887.
[53] A. Deschamps, Y. Brechet, Influence of predeformation and agEing of an Al–Zn–Mg alloy—II. Modeling of precipitation kinetics and yield stress, Acta Materialia. 47 (1998) 293–305. https://doi.org/10.1016/S1359-6454(98)00296-1.
[54] Z.N. Farhat, Y. Ding, D.O. Northwood, A.T. Alpas, Effect of grain size on friction and wear of nanocrystalline aluminum, Materials Science and Engineering: A. 206 (1996) 302–313. https://doi.org/10.1016/0921-5093(95)10016-4.
[55] W. Lefebvre, N. Masquelier, J. Houard, R. Patte, H. Zapolsky, Tracking the path of dislocations across ordered Al3Zr nano-precipitates in three dimensions, Scripta Materialia. 70 (2014) 43–46. https://doi.org/10.1016/j.scriptamat.2013.09.014.
[56] T. Uesugi, K. Higashi, First-principles studies on lattice constants and local lattice distortions in solid solution aluminum alloys, Computational Materials Science. 67 (2013) 1–10. https://doi.org/10.1016/j.commatsci.2012.08.037.
[57] A.J. Ardell, Precipitation hardening, Metall Mater Trans A. 16 (1985) 2131–2165. https://doi.org/10.1007/BF02670416.
[58] C.B. Fuller, D.N. Seidman, D.C. Dunand, Mechanical properties of Al(Sc,Zr) alloys at ambient and elevated temperatures, Acta Materialia. 51 (2003) 4803–4814. https://doi.org/10.1016/S1359-6454(03)00320-3.
[59] S. Thangaraju, M. Heilmaier, B.S. Murty, S.S. Vadlamani, On the Estimation of True Hall–Petch Constants and Their Role on the Superposition Law Exponent in Al Alloys, Advanced Engineering Materials. 14 (2012) 892–897. https://doi.org/10.1002/adem.201200114.
[60] K.L. Kendig, D.B. Miracle, Strengthening mechanisms of an Al-Mg-Sc-Zr alloy, Acta Materialia. 50 (2002) 4165–4175. https://doi.org/10.1016/S1359-6454(02)00258-6.
[61] W. Lefebvre, G. Rose, P. Delroisse, E. Baustert, F. Cuvilly, A. Simar, Nanoscale periodic gradients generated by laser powder bed fusion of an AlSi10Mg alloy, Materials & Design. 197 (2021) 109264. https://doi.org/10.1016/j.matdes.2020.109264.
[62] A. Mehta, L. Zhou, T. Huynh, S. Park, H. Hyer, S. Song, Y. Bai, D.D. Imholte, N.E. Woolstenhulme, D.M. Wachs, Y. Sohn, Additive manufacturing and mechanical properties of the dense and crack free Zr-modified aluminum alloy 6061 fabricated by the laser-powder bed fusion, Additive Manufacturing. 41 (2021) 101966. https://doi.org/10.1016/j.addma.2021.101966.
[63] R.J. Arsenault, N. Shi, Dislocation generation due to differences between the coefficients of thermal expansion, Materials Science and Engineering. 81 (1986) 175–187. https://doi.org/10.1016/0025-5416(86)90261-2.

[64] B. Derby, J.R. Walker, The role of enhanced matrix dislocation density in strengthening metal matrix composites, Scripta Metallurgica. 22 (1988) 529–532. https://doi.org/10.1016/0036-9748(88)90019-1.
[65] P. Maurya, N. Kota, J. Gibmeier, A. Wanner, S. Roy, Review on study of internal load transfer in metal matrix composites using diffraction techniques, Materials Science and Engineering: A. 840 (2022) 142973. https://doi.org/10.1016/j.msea.2022.142973.
[66] V.C. Nardone, K.M. Prewo, On the strength of discontinuous silicon carbide reinforced aluminum composites, Scripta Metallurgica. 20 (1986) 43–48. https://doi.org/10.1016/0036-9748(86)90210-3.

APPENDIX A

The various equations employed to provide estimates of the contributions of the various strengthening mechanisms of the Al matrix are given hereafter so that the interested reader can easily reproduced the calculations reported in this work.

The contribution of order strengthening is given by equation (A-1).

$$\varDelta\sigma_{Ord} = 0.81M\frac{\gamma_{APB}}{2b}\left(\frac{3\pi f_v}{8}\right)^{\frac{1}{2}} \qquad (A-1)$$

with M the Taylor factor, γ_{APB} the antiphase boundary, b the Burgers vector of FCC Al and f_v the volume fraction of nanoprecipitates estimated by SAXS.

The contribution of coherency strengthening can be estimated using equation (A-2).

$$\varDelta\sigma_{Coh} = M\alpha_{Coh}(G\theta)^{\frac{3}{2}}\left(\frac{\langle R\rangle f_v}{0.5Gb}\right)^{\frac{1}{2}} \qquad (\mathrm{A}-2)$$

G is the shear modulus of the matrix FCC Al, α is a constant, θ is the constrained lattice parameter mismatch at RT taken here $\approx(2/3)\delta$ where δ is the lattice parameter mismatch, and $\langle R\rangle$ the average size of the nanoprecipitates estimated using SAXS.

The strengthening brought by the difference in modulus between the matrix and the precipitate can be estimated using equation (A-3).

$$\varDelta\sigma_{Mod} = 0.0055M(\varDelta G)^{\frac{3}{2}}\left(\frac{2f_v}{Gb^2}\right)^{\frac{1}{2}} b\left(\frac{\langle R\rangle}{b}\right)^{\left(\left(\frac{3m}{2}\right)-1\right)} \qquad (\mathrm{A}-3)$$

$\varDelta G$ is the difference in shear modulus between the matrix FCC Al and the $L1_2$-Al_3Zr nanoprecipitates and m a constant.

Finally, when obstacles are not sheared by dislocations, they are bypassed. In this case, the contribution to the yield strength can be calculated using equation (A-4).

$$\varDelta\sigma_{Oro} = M\frac{0.4Gb}{\pi\sqrt{1-\nu}}\frac{(ln\, 2\langle R\rangle/b)}{\lambda_p} \qquad (\mathrm{A}-4)$$

With ν the Poisson ration of FCC Al and $\lambda_p = 2\langle R\rangle\left(\sqrt{\frac{\pi}{4f_v}}-1\right)$ is the mean edge-to-edge interparticles spacing.